

DISORDER EFFECT IN GRAPHENE AND TOPOLOGICAL
INSULATOR

By

DONGWEI XU

Bachelor of Science in Physics
Lanzhou University
Lanzhou, Gansu, China
2005

Master of Science in Physics
Lanzhou University
Lanzhou, Gansu, China
2007

Submitted to the Faculty of the
Graduate College of
Oklahoma State University
in partial fulfillment of
the requirements for
the Degree of
DOCTOR OF PHILOSOPHY
July, 2012

COPYRIGHT ©

By

DONGWEI XU

July, 2012

DISORDER EFFECT IN GRAPHENE AND TOPOLOGICAL
INSULATOR

Dissertation Approved:

Dissertation Advisors Name Here

Dissertation Advisor

Committee Member Name Here

Committee Member Name Here

Committee Member Name Here

Grad. College Dean's Name Here

Dean of the Graduate College

TABLE OF CONTENTS

Chapter		Page
1	INTRODUCTION	1
1.1	Disorder	1
1.1.1	Disorder Types	1
1.1.2	Localization	3
1.1.3	Scaling Theory	4
1.2	Introduction of Graphene	6
1.2.1	Overview	6
1.2.2	Structure, Properties and Applications	6
1.2.3	Stacking Order for Multilayer Graphene	10
1.2.4	Fabrication	11
1.3	Topological Insulator (TI)	12
1.3.1	Overview: Definition and Characterization	12
1.3.2	TI Materials	13
1.3.3	General Theory for Topological Insulator	14
1.4	Organization	15
2	DISORDER INDUCED FIELD EFFECT TRANSISTOR IN BI-LAYER AND TRILAYER GRAPHENE	16
2.1	Introduction	16
2.2	Model	18
2.3	Results and Discussion	20
2.3.1	Electron Transport in Bilayer Graphene	20

2.3.2	Four Band Model for Bilayer Graphene	27
2.3.3	Trilayer Graphene with two Different Stacking Orders	29
2.4	Conclusion	32
3	PHASE STRUCTURE OF THE TOPOLOGICAL ANDERSON IN-	
	SULATOR	36
3.1	Introduction	36
3.1.1	The TAI Model	40
3.2	The Phase Diagram in Systems of Size $L \leq 280a$	42
3.2.1	The TAI Conductance Plateau	42
3.2.2	Phase Diagram	48
3.2.3	Bulk State Delocalization and Fractality	52
3.3	Infinite Volume Limit	54
3.3.1	Transition from Bulk Conduction to the TAI Plateau	56
3.3.2	Localization Transitions	57
3.3.3	Infinite Volume Limit of the Gapped TAI-I Scaling Region	60
3.3.4	Conductance Distributions at the Phase Transitions	64
3.4	Conclusion	67
4	CONCLUSIONS	70
	BIBLIOGRAPHY	72

LIST OF TABLES

Table		Page
1.1	Number of articles vs. year ('Web of knowledge' database)	6

LIST OF FIGURES

Figure		Page
1.1	Different sorts of disorder. (a) Perfect ordered limit. (b) Identical atoms sitting at random positions represent structural disorder. (c) When the number of nearest neighbors is constant the system is called topologically disordered. (d) Two different kinds of atoms sitting at the sites of an ideally ordered lattice represent the simplest case of compositional disorder. (e) An assembly of randomly oriented spins is a typical example of an orientationally disordered system. (f) A regular lattice of identical atom connected with two different kinds of hopping matrix elements is the most simple case of a system with randomness in the kinetic energy. This figure is from Ref. [1]	2
1.2	The sechematic figure for mobility edge. The mobility edge separate electronic localized state and extended state. This figure is from Ref. [1]	3
1.3	β -function vs. $\ln g$ for different dimensions. This figure is from Ref. [2]	5
1.4	Graphene's band dispersion and low energy Dirac cone. Conductance and valence band touch at the K and K' point. The energy momentum dispersion relation becomes linear in the vicinity of those points and the dispersion relation is relativistic with an effective mass being zero. This figure is reproduced from Ref. [3].	7
1.5	Structures of armchair (left) and zigzag (right) edged graphene nanoribbons. Get from web: (http://www.graphenelitreviews.blogspot.com/)	8

2.1	(a) Schematic diagram of bilayer graphene supported by a substrate. (b) Voltage $+U$ is applied to the bottom layer while $-U$ to the top layer. (c) Voltage $-U$ is applied to the bottom layer while $+U$ to the top layer. The black coloring in figures (b) and (c) represents disorder caused by the bottom layer's coupling to the substrate	18
2.2	Conductance and relative conductance ratio (G_{+U}/G_{-U}) of zigzag edged bilayer graphene as a function of Fermi energy. The effect of Anderson (bond) disorder is shown in the upper (lower) panels. (a) and (d) are the conductances G_{+U} when voltage $+U$ ($-U$) is applied to bottom (top) layer (as the bias voltage applied in Fig. 2.1b). (b) and (e) are the conductances G_{-U} when voltage $-U$ ($+U$) is applied to the bottom (top) layer (as the bias voltage applied in Fig. 2.1c). The parameter $U = 0.03t$. (c) and (f) are the ratio of the conductances obtained from the above two opposite voltages. Different colors (line types) represent different disorder strengths as labeled in (f).	22
2.3	Conductance ratio (G_{+U}/G_{-U}) of zigzag bilayer graphene as a function of Fermi energy. The effect of asymmetric Anderson (bond) disorder is shown in the up (lower) panels. The disorder strength W is $0.5t$ in (a) and (c), $1.2t$ in (b) and (d). Different colors (line types) represent different bias voltages U as labeled in (d). The vertical dashed lines $U1$, $U2$, $U3$ and $U4$ are guide lines corresponding to the condition $E = U$, which are $0.05t$, $0.08t$, $0.12t$, and $0.2t$ respectively.	24

- 2.4 Conductance ratio (G_{+U}/G_{-U}) of armchair bilayer graphene. Different bias voltages are applied: (a) $U = 0.03t$, (b) $U = 0.08t$, (c) $U = 0.12t$ and (d) $U = 0.2t$. The conductance ratio is truncated inside the gap, i.e., smaller than the Fermi energy $0.0279t$, $0.0547t$, $0.0635t$ and $0.0701t$ for different applied voltages $0.03t$, $0.08t$, $0.12t$ and $0.2t$ respectively (referring to the dispersion in Fig. 2.5). The different line colors (line types) indicate different disorder strengths as labeled in (c). The inset in (d) gives the conductances for different disorder strengths at $U = 0.2t$. 26
- 2.5 Dispersion and LED of bilayer graphene. Different bias voltages are applied: (a) $U = 0.03t$, (b) $U = 0.08t$, (c) $U = 0.12t$ and (d) $U = 0.2t$. The signs ‘+’ and ‘-’ in (d) indicate the direction of the bands moving with the voltage. (e)-(h) show the LED corresponding to the dispersion in (a)-(d). The red solid and blue dashed lines indicate the LED in layers applied voltage $+U$ and $-U$ respectively. The shaped region ‘H’ indicate the existence of a single band. 30
- 2.6 Dispersion and LED of trilayer graphene. Bias voltages $U = 0.08t$ (upper panels) and $U = 0.2t$ (lower panels) are applied. (a) and (c) show the energy dispersion for ABA stacking. (b) and (d) show the dispersion for ABC stacking. The black horizontal dashed lines represent the critical changes of energy bands. (e)-(h) give the LED in the layer applied voltage $-U$ (blue dot lines) or $+U$ (red solid lines). The black vertical dashed lines in (e)-(h) give the same Fermi energies as the black horizontal dashed lines indicated in (a)-(d). 33

2.7	Conductance ratio of zigzag edged ABA (left panels) and ABC (right panels) stacked trilayer graphenes. Different bias voltages are applied: $U = 0.08t$ in (a) and (b), $U = 0.2t$ in (c) and (d). The different line colors (line types) indicate different disorder strengths. The black vertical dashed lines correspond to the same critical Fermi energies as shown in Fig. 2.6.	34
3.1	Two TAI scaling regions: TAI-I with only edge states, and TAI-II with both edge states and localized conducting states. Lines $W1$ and $W3$ mark the edges of the TAI conductance plateau, and $W2$ marks the boundary between the gapped TAI-I scaling region on the left and the ungapped TAI-II scaling region on the right. Panes a, b, and c show respectively the conductance, the scaled distance from the edge, and La times the local density of states. The CPA ($L = 200a$) lines report the results of the coherent potential approximation. The Fermi energy is fixed at $E = 12$ meV.	44
3.2	TAI Conductance Quantization without a Band Gap. The disorder strength is fixed at $W = 200$ meV. $E1$ and $E2$ label crossing points which mark the edges of the conductance plateau. The local density of states ρ is independent of system size L , indicating that it is dominated by bulk states. The conductance gap near $E = 0$ is caused by the disorder-free leads, which do not conduct at $ E \leq 1$ meV. The ‘ $L=200a(\text{doped})$ ’ line shows clearly that when the leads are doped to $E = 25$ meV the conductance plateau extends to the $E1$ crossing point.	46

3.3	The TAI phase diagram at mass $M = 1$ meV. In Regions I A and I B the bulk states conduct. An Anderson transition separates Region I B from Region II, where the system is insulating. The TAI conductance plateau includes both the gapped TAI-I region (colored blue) and the ungapped TAI-II region (hatched lines.) The region inside the dashed lines to the left of line m is gapped and has no surface states. This phase diagram reflects only physics at length scales $L \leq 280a$	51
3.4	Eigenstate hyperlocalization near the mean-field band edge. Inside the colored ‘PR’ area the average PR is very small. (In this plot we show the region where $\langle PR \rangle \leq e^5 a^2 \approx 148a^2$ at system size $L = 200a$.) If we omit surface states from the average, then we find that the bulk states are hyperlocalized in both the gapped TAI-I region and the PR region. Lines $b1$ and $b2$ show where the CPA-adjusted Fermi level crosses the CPA-adjusted band edges, and match well with the bulk hyperlocalized region. The lower right inset shows the average participation ratio at four system sizes, while the upper right inset shows the fractal dimension. The Fermi energy is fixed at $E_F = 12$ meV in both insets.	55
3.5	Phase transitions from the bulk conducting phase to the TAI-I and TAI-II scaling regions. Panes a and c show the transition to the gapped TAI-I scaling region, while panes b and d show the transition to the ungapped TAI-II scaling region. The insets show closeups of the conductance data. The straight lines in the upper right inset are least squares linear fits to the data.	58

3.6	Anderson transitions to the localized phase. Panes a and c show the transition from the TAI conductance plateau to the insulating phase, while panes b and d show the transition from the bulk conducting phase to the insulating phase. The insets show the crossing points in a larger perspective. The vertical lines show the phase transition boundaries obtained using sizes $L = 50, 100, 200a$ (same as Figures 3.1 and 3.3).	61
3.7	The TAI-I scaling region at large volumes. The density of states converges as the system size increases, starting at the edges of the TAI-I scaling region near $W \approx 110, 130$ meV and moving into the center of the scaling region. This convergence indicates that bulk states dominate the DOS in the infinite volume limit. The converged DOS agrees well with the ‘PBC’ lines, which were obtained with periodic boundary conditions and report the DOS of bulk states only. The converged value of the bulk DOS is roughly linear on both sides of the TAI-I scaling region, which indicates that the bulk DOS is exponentially small, as is typical of Lifshitz tails.	63

3.8 Conductance distributions at the TAI phase transitions. Pane a: the TAI bulk conduction-quantized transition, compared to the quantum spin Hall metal-quantized transition. Pane b: the TAI quantized-insulator transition, compared to the IQH with open boundary conditions. Pane c: the TAI bulk conduction-insulator transition at $W = 90$ meV, compared to the Quantum Spin Hall metal-insulator transition. Pane d: the TAI bulk conduction-insulator transition at $W = 95$ meV, compared to the IQH with periodic boundary conditions. We rescaled Kobayashi et al's QSH data by a factor of 2 ($P(G) \rightarrow 2P(G/2)$) because in our own calculations we report only $1/2$ of the total conductance of the 4×4 Hamiltonian - see the discussion in section 3.1.1. The system size is $L = 200a$ for all of our distributions. 66

CHAPTER 1

INTRODUCTION

1.1 Disorder

1.1.1 Disorder Types

In reality, there are no ideally ordered media. There are always distortions of the ideal order due to the presence of impurities, dislocations, vacancies and other defects. There are two limiting cases of short- and long-range potential disorder. Depending on how the correlations decay with distance, one speaks of long-range order or short-range order. The short-range impurity is equivalent to a potential shift at a particular lattice site. Long-range order characterizes physical systems exhibiting correlated behavior; the scattering length is large in comparison with the lattice constant but is still smaller than the Fermi wavelength.

Fig. 1.1 gives the models of disorder constructed from ideal crystal. For glassy systems and amorphous semiconductors, the disorder model may be obtained by relaxing the lattice structure (structural disorder). For alloy whose lattice are two or more different kinds of atoms, it may be modeled by Fig. 1.1d. Disorder can be introduced by taking the site energies and/or the hopping matrix elements at random with some probability distribution to the initial Hamiltonian. The on-site energy fluctuation models the Anderson disorder while the hopping matrix models the bond disorder. In Chap. 3, we consider the topological insulator induced by Anderson disorder. In Chap. 2, both Anderson and bond disorders are taken into account in multilayer graphene. Magnetic disorder is not considered in our work.

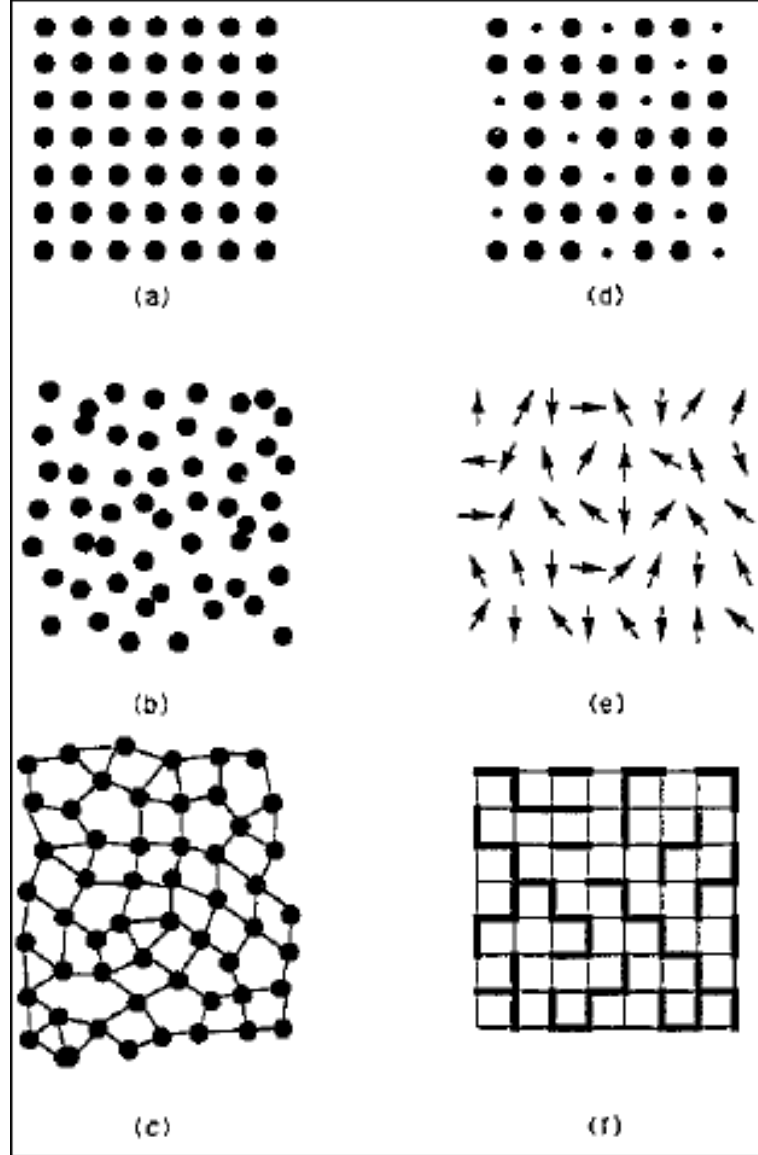


Figure 1.1: Different sorts of disorder. (a) Perfect ordered limit. (b) Identical atoms sitting at random positions represent structural disorder. (c) When the number of nearest neighbors is constant the system is called topologically disordered. (d) Two different kinds of atoms sitting at the sites of an ideally ordered lattice represent the simplest case of compositional disorder. (e) An assembly of randomly oriented spins is a typical example of an orientationally disordered system. (f) A regular lattice of identical atom connected with two different kinds of hopping matrix elements is the most simple case of a system with randomness in the kinetic energy. This figure is from Ref. [1]

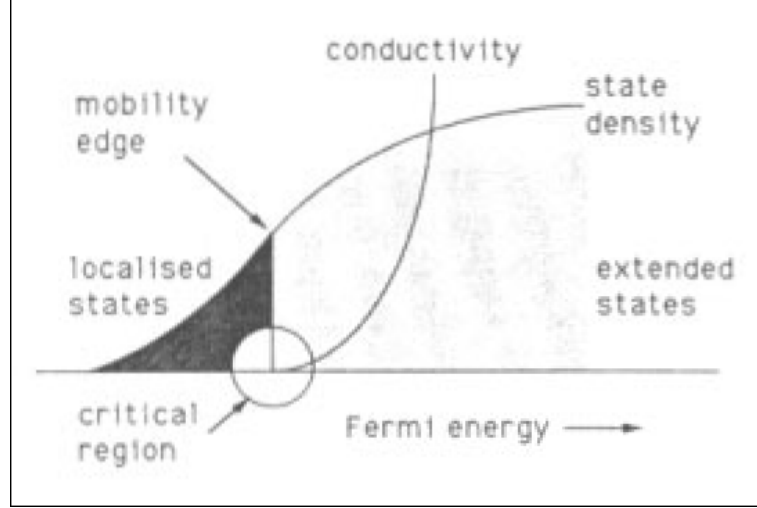


Figure 1.2: The schematic figure for mobility edge. The mobility edge separates electronic localized states and extended states. This figure is from Ref. [1]

1.1.2 Localization

In disordered systems there are two important length scales: the scattering length, and the localization length which is typically much longer. The scattering length scale regulates the density of states, while the localization length scale regulates conduction and localization. The localization properties of the states influence the transport properties of the system. In a perfect crystal lattice maintaining the translational symmetry, the wave function of the electron is an extended Bloch wave. When the disorder strength is strong enough, the extended wave will be localized in space. The localization comes from the quantum mechanical backscattering on the random potential on the lattice, which induces destructive interference of the wave function with itself. Localized states do not contribute to transport. The Anderson model [4] of localization describes the quantum mechanical motion of an electron on a lattice with a random potential without any thermal activation.

Based on the Anderson model, Mott [5] proposed the concept of mobility edge to separate the localized states from the extended states. Fig. 1.2 is the sketch

map. The mobility edge depends on the disorder. With the increase of disorder strength, the delocalized state near the Fermi energy can be localized. Beyond some critical disorder, all the states are localized and the system is insulating at $T=0$. This transition from a metallic to an insulator system induced by the disorder is called Anderson transition.

In Kramer's paper [1], they summarized seven definitions of localization: (1) Asymptotic behavior of wavefunction. The asymptotic behavior is described by the localization length λ . Infinite localization length corresponds to an extended state. (2) The inverse participation number. The inverse participation ratios (IPRs) [6] are defined as $P_q = \int d^d \vec{r} |\psi(\vec{r})|^{2q}$ where d represents the dimensionality. It can be used to characterize the extension of eigenfunctions. For an extended state, P_q is proportional to L^d , while for a localized state, P_q is a constant beyond a certain system size. From P_q , the fractal dimensionality D_q can be defined via $\langle P_q \rangle = L^d \langle |\psi(\vec{r})|^{2q} \rangle \sim L^{-D_q(q-1)}$. L is the system size. In a metal $D_q = d$, in an insulator $D_q = 0$, while at a critical point D_q is a nontrivial function of q , implying wavefunction multifractality. In Chap. 3, we use these two parameters to characterize the topological phase. (3) Absence of diffusion. (4) Transmission through random potential. (5) Absence of diffusion and inverse participation number. (6) Sensitivity to boundary condition. Localized states do not feel the boundaries due to their exponential decay, while in the metallic regime, the eigenvalues are influenced even for infinite system size. (7) Lyapunov exponents.

1.1.3 Scaling Theory

The essential hypothesis of the scaling theory is that in the vicinity of the transition between localized and extended states there is only one relevant scaling variable which is sufficient to describe the critical behavior [7]. Physically, this is equivalent to the statement that close to the transition it does not make any sense to distinguish between the various mechanisms for localization. To describe the scaling behavior,

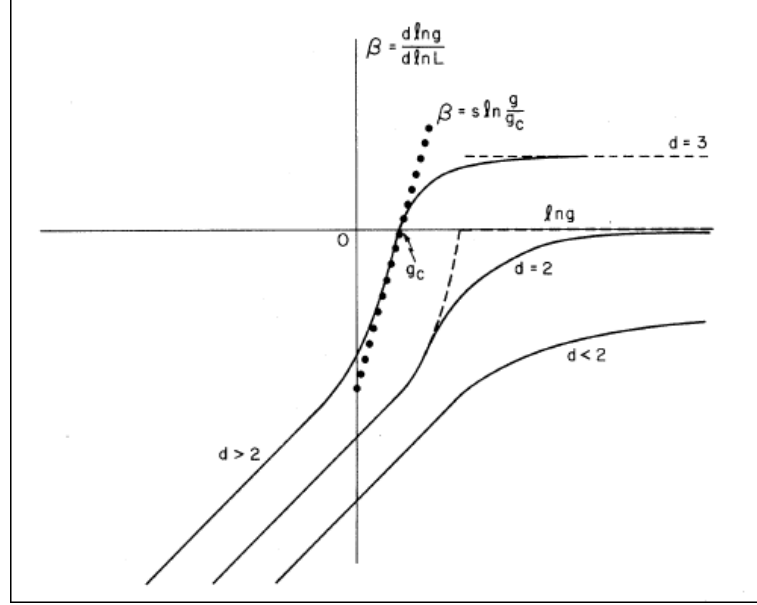


Figure 1.3: β -function vs. $\ln g$ for different dimensions. This figure is from Ref. [2]

β -function is defined as $\beta(g) = \frac{d \ln g}{d \ln L}$, where g is a dimensionless parameter characterizing the conductance and L the size of d -dimensional system. For large conductance, $g \propto L^{d-2}$, resulting $\beta(g) = d - 2$. For small conductance, $g \propto \exp(-L/\lambda)$ and then $\beta(g) \propto \ln g$.

Fig. 1.3 shows the behavior of β -function for different dimensions. In dimension larger than 2, there exists a critical point between metallic and insulator phase. In dimension less than two, the electrons are localized for any disorder with finite localization length. In 2D, weak disorder can localize the electrons, but the localization length can be exponentially large. From the figure, one can conclude that metal-insulator transition can only happen in dimension $d > 2$. In Abrahams and coworker's statement [2], no true metallic state in 2D, and no metal-insulator transition either. In fact, the effects of interactions are not easy to handle theoretically. In experiment, metal-insulator transition in two dimensional electron system has been observed for interacting electrons [8, 9]. Several theoretical explanations have been taken [8, 9, 10, 11, 12]. It seems Punnoose and Finkelstein's [11] theory is more

reasonable, i.e., a true quantum critical point exists. In Chap. 3, we take a research relating to the phase transition in 2D system.

1.2 Introduction of Graphene

1.2.1 Overview

Graphene, as a single atomic layer of graphite, consists of carbon atoms arranged in a two-dimensional (2D) honeycomb lattice. It is the basic building block for graphitic materials. The 2010 Nobel Prize in physics was awarded to Andre Geim and Konstantin Novoselov for their breakthrough ‘finding’ of graphene. In their work, graphene samples were separated through the micro-mechanical cleavage of graphite. Since then, graphene has attracted extensive research interest from all over the world. Table I shows the numbers of articles containing the term ‘graphene’ in title according to the ‘Web of knowledge’ database in the last ten years. It is obvious from this table that graphene attracts more and more interest in the past decade.

Table 1.1: Number of articles vs. year (‘Web of knowledge’ database)

Year	2002	2003	2004	2005	2006	2007	2008	2009	2010	2011
Number of articles	7	12	23	33	155	642	1267	3213	5534	8155

1.2.2 Structure, Properties and Applications

Graphene is the first 2D atomic crystal ever known [13]. In the past, 2D crystals were believed to be only a theoretical model which should not exist in reality [14]. The insight was that thermal fluctuation would be the destroyer, which made 2D material unstable. In fact, the melting temperature of thin films decreases quickly when the thicknesses decrease [15]. Typically, thin films become unstable when the number of

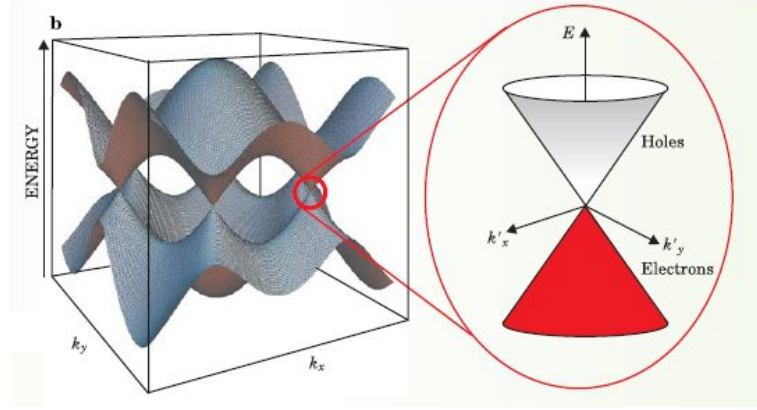


Figure 1.4: Graphene's band dispersion and low energy Dirac cone. Conductance and valence band touch at the K and K' point. The energy momentum dispersion relation becomes linear in the vicinity of those points and the dispersion relation is relativistic with an effective mass being zero. This figure is reproduced from Ref. [3].

atomic layers falls below a few dozens. This is why we call Geim and Novoselov's work a 'breakthrough' experiment. The accordance of theory with experiment can be understood by noting that graphene is quenched in a metastable state from 3D graphite. Beyond graphene, a variety of atomic-thin 2D materials have been prepared by micromechanical exfoliation (e.g., BN, MoS₂, BbSe₂ and Bi₂Sr₂CaCu₂O_x), surface assisted in-situ growth (e.g., BN) and exfoliation into colloidal solutions (e.g., MnO₂ and Eu(OH)_{2.5}(DS)_{0.5}) [16]. Like graphene, these 2D materials share a common property that the corresponding 3D counterpart has a layered structure. It is formed by covalent bonds in-plane, while it is stabilized by weak van der Waals interactions inter-plane.

As one sub-nano 2D material, graphene exhibits a variety of peculiar properties. Although it is the thinnest crystal, graphene is known as the strongest material ever. The strong sp² hybridized carbon-carbon bonds result in an ultra-high breaking strength, which is about 200 times than that of steel [17]. Yet, graphene shows a great flexibility in deformation. It can sustain a 20 % in-plane strain. What's more, as a

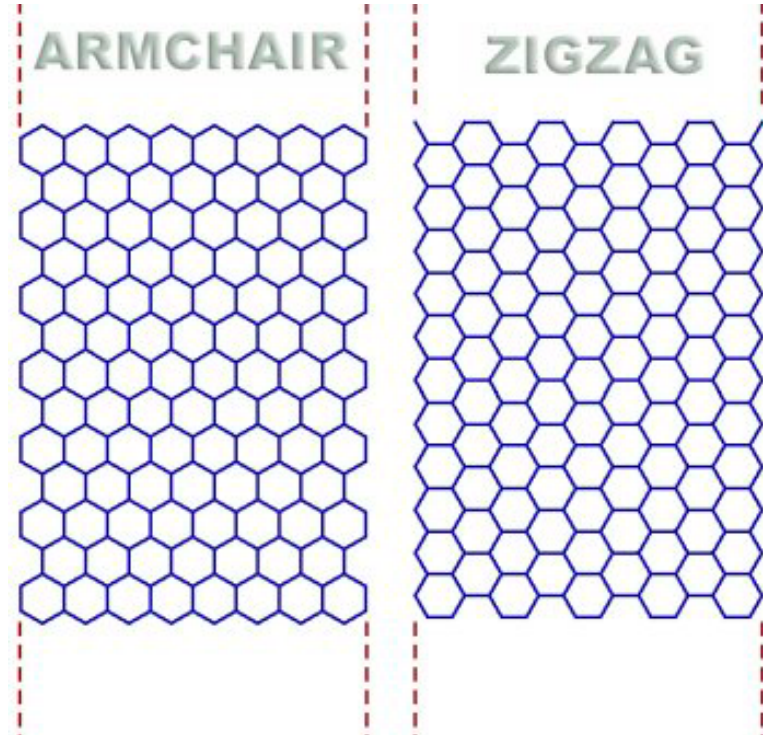


Figure 1.5: Structures of armchair (left) and zigzag (right) edged graphene nanoribbons. Get from web: (<http://www.graphenelitreviews.blogspot.com/>)

2D crystal, graphene also shows a great pliability. Electronically, the E-k dispersion is linear at the Dirac cone (Fig. 1.4). The conduction band and valence band meet at the Dirac cone, making graphene a zero-gap semiconductor. The charge carriers in graphene are massless Dirac fermions [13, 18]. Electrically, graphene is more conductive than silver. Electrons in graphene can travel for micrometers without scattering. Accordingly, the electron mobility of graphene can reach as high as $106\text{cm}^2/\text{Vs}$ at room temperature, which is about 70 times higher than that of silicon [19]. This high electron mobility, combining with the ability to integrate well with other materials, makes graphene promising materials for the high-frequency analogue electronics. Thermally, graphene overperforms carbon nanotubes in thermal conduction. At room temperature, the thermal conductivity of graphene is about $5 \times 10^3\text{W}/\text{mK}$ [20], compared with $3.5 \times 10^3\text{W}/\text{mK}$ for singled-walled carbon nanotubes.

Edge modification may change the dimensionality of graphene. A pristine graphene monolayer can be cut into elongated strips to form quasi-1D structure, referred to as graphene nanoribbons (GNRs) which can be terminated by either armchair or zigzag edges (Fig. 1.5). GNRs can be either metallic or semiconducting depending on the type and width of edges [18]. In Chap. 2, these two kinds of edges are considered. Substrate is another factor which may significantly modify graphene's properties. When graphene is epitaxially grown on SiC, a finite energy gap of 0.26eV was opened. [21] When graphene is deposited on SiO_2 substrate, spatially dependent perturbation on the structure was observed [22]. On the other hand, graphene on BN substrate behaves like freestanding graphene, exhibiting ultra-high electron mobility [23]. In Chap. 2, disorder from substrate is paid much attention.

Like other materials, the application of graphene is closely related to its properties. In the following some promising applications of graphene are listed. (1) Graphene Field Emission (FE) display. FE is the process in which electrons are emitted in the presence of high electric field. To create such high field, graphene is required to be erected on the substrate. Eda et al. have succeeded in synthesizing a graphene based cathodes [24]. However, it still needs time to reach market. (2) Graphene based gas and bio sensors. This is one of the most promising applications of graphene. The corresponding scheme is, on absorption of atoms or molecules to graphene surface, the electronic transport property of graphene is changed. The absorbed molecules work as either donors or acceptors. For example, Schedin demonstrated graphene is sensitive to NO_2 , NH_3 , H_2O and CO [25]. Gowtham has shown graphene exhibits different affinity to different nucleobases, evidenced by different binding energies [26]. (3) Transparent electrodes. Graphene is transparent across the spectrum, allowing 97.7 % of light to get through [27]. As a consequence, graphene is of great potential of working as transparent electrodes in touch screens and solar cells. (4) Bionics application. Graphene can also be applied in bionics due to two advantages [28]. On

one hand, it is impervious to ionic solutions in human body. On the other hand, it can conduct electrical signals, enabling interfacing with the nervous system.

1.2.3 Stacking Order for Multilayer Graphene

Graphene is the constituent element of graphite, which is a 3D bulk. Typically, graphite has an AB (Bernal) stacked structure. Although AA stacked graphite has been reported experimentally [29], AB stacking is more stable in terms of interlayer coupling [30]. In this paper we only consider Bernal stacking between adjacent layers in graphite or bilayer and trilayer graphene. One can imagine when graphenes are AB stacked together, they finally recover the properties of bulk graphite once the number of layers is large enough. It was confirmed that if the number of stacked graphene layers fell below 10, the stacked structure should be considered as a 2D crystal, rather than a 3D material [13]. Typically, 2D graphene materials are classified into three categories, i.e., monolayer graphene, bilayer graphene and few-layer (3 to < 10) graphene. Besides monolayer, bilayer graphene also gains extensive study both theoretically and experimentally for its interesting properties. The most notable property of bilayer graphene is its ability of opening a tunable gap when a perpendicular electric field is applied [31, 32]. This property is essential to fabricating graphene-based switchable devices such as field effect transistors (FETs). At ground state, bilayer graphene is a zero-gap semiconductor. When a perpendicular electric field is applied, the broken inversion symmetry results in a finite energy gap. The opened energy gap is linear with low field, and finally gap saturates at about 250meV [32]. Trilayer graphene is more interesting than bilayer graphene due to its more stacking formats. Recently, trilayer graphene was shown to exhibit stacking dependent gap tunability. At ground state, like the monolayer and bilayer counterparts, trilayer graphene is gapless. In the presence of electric field, ABA stacked graphene is still metallic while ABC stacked graphene becomes insulating [33].

1.2.4 Fabrication

The producing and observing monolayer graphene started from Geim and Novoselov's pioneering work [34, 13], as mentioned above. In fact, the realization of graphene samples was not as difficult as identifying samples' parameters (e.g., size and number of layers). Geim and Novoselov's success lay in the fact that graphene on SiO_2 becomes visible with the help of an optical microscope. Later, Raman spectroscopy was also found to be able to identify graphene [35]. Graphene can be isolated by a number of methods. (1) Micromechanical exfoliation of graphite [34, 13]. This was done by either rubbing graphite crystals against each other or by means of an adhesive tape. The obtained ordered structure has a dimension of about $10\mu\text{m}$ by $100\mu\text{m}$. (2) Liquid phase exfoliation of graphite. This approach takes use of surface-active organic liquids [36]. The exfoliation of graphite becomes easier when small atoms or molecules are allowed to penetrate graphite, which increases the interlayer spacings of graphite. (3) Graphite oxidation. Chemical oxidizers can also aid graphite exfoliation [37, 38]. Inner graphite layers are first oxidized in the presence of oxygen or halogens, which decreases the interlayer coupling strength. Then, a subsequent reduction reaction is required to obtain graphene. (4) Chemical vapor deposition (CVD). The CVD method is also one most popular approach in producing carbon nanotubes [39]. One example of applying CVD to synthesizing graphene used Ni film as the substrate, which worked as the catalyst [40]. The synthesis was performed in a quartz tube at a temperature of 1000°C . (5) Epitaxial growth on a metal surface. Ru(0001) surface can be utilized as a substrate [41]. The synthesis of graphene was in high-vacuum conditions. Moiré pattern was observed which was related to dispersive van der Waals interactions [42].

1.3 Topological Insulator (TI)

1.3.1 Overview: Definition and Characterization

Topology is a branch of mathematics that studies the properties of objects which are invariant under smooth deformations. In physics, TIs [43] are electron systems that behaves as an insulator in the bulk state while conducting on their surface (edge) states. Different from normal insulator, the topologically protected surface (edge) state is robust against impurities or imperfections.

Traditionally, symmetry is used to classify different phases. However, it does not work in TI. For instance, quantum hall states at different filling factor have different hall conductance, but they hold the same symmetry. A new parameter, topological order [44] works in classifying different topological states. It defines a topological phase which is insensitive to smooth changes of the material parameters and cannot change unless a quantum phase transition happens. Two insulating state are different if they cannot adiabatically change into each other. The topological order is related to some discrete numbers in the sense of discontinuity. For systems without time reversal symmetry, the Chern number is used to characterize the topological order. It is mathematically expressed as the winding number of the Berry phase of electron wavefunctions around the Brillouin zone. We call time reversal breaking systems as integer-class Chern-Simons insulators. For systems protected by time reversal system, where the Chern number is always zero, Z_2 [45, 46, 47, 48] is employed to characterize the time reversal invariant band structures. This Z_2 insulator is symmetry protected TI.

Two related studies are quantum hall effect and quantum spin hall effect. Quantum Hall effect [49] corresponds to the quantum version of the Hall effect, with the quantized Hall conductance of a 2D electron gas system in low temperature and large magnetic field. The magnetic field breaks the time reversal symmetry, implying that

the topological order is characterized by the Chern number. The Hall conductance is an integer multiple of a fundamental constant e^2/h . This integer is equal to the Chern number in mathematics. For quantum spin Hall effect [50, 51, 52, 53], the time reversal is invariant as there is no magnetic field. The spin is locked with the momentum. Spin up and spin down states counter-propagate at the edge and the back-scattering between left and right moving edge states is forbidden due to Kramers degeneracy. The quantum spin Hall insulator is a new state of matter which is characterized by Z_2 . In two dimensions, there is a single Z_2 invariant that distinguishes the ordinary insulator ($Z_2 = 0$) from the quantum spin-Hall phase ($Z_2 = 1$).

By definition, a 3D TI [54] has an insulating bulk and conducting surfaces, distinguishing 2D with edge state. The first 3D TI to be identified experimentally was the semiconducting alloy $\text{Bi}_{1-x}\text{Sb}_x$ [55]. There are two kinds of TI in 3D: weak TI and strong TI. A weak TI is topologically equivalent to stacking layers of the 2D TI along a certain direction. Nontrivial surface states only exist in the surface parallel to the stacking direction. There is no big difference from 2D TI. The strong TI is intrinsically 3D and has helical surface states in any surfaces. In three dimensions, there are four Z_2 invariants that distinguish the ordinary insulator from ‘weak’ and ‘strong’ topological insulators. The difficulty of 3D TI is that the bulk of any TI is not completely insulating even at very low temperature.

1.3.2 TI Materials

Many 2D and 3D TI materials [56, 57] have been theoretically predicted and experimentally realized in a variety of systems. The first several materials discovered include HgTe/CdTe quantum wells [58, 59], $\text{Bi}_{1-x}\text{Sb}_x$ alloy [60, 55] and the family of Bi_2Te_3 , Bi_2Se_3 , and Sb_2Te_3 crystals [61, 62, 63]. The common experimental techniques to study the TI materials are Angle-Resolved Photo-Emission (ARPES), Scanning Tunneling Microscopy (STM), etc.

There are some new defined TIs, e.g., topological Mott insulator (TMI) and topological Anderson insulator (TAI). For strongly interacting topological insulators, dynamic generation of spin-orbit coupling can give rise to TMI [64]. The TMI states can be understood in the framework of the topological order parameter expressed in terms of the full Green's function [65]. For disordered systems, new topological order can be induced by disorder from normal insulator or metal [66, 67, 68, 69, 70], which is called TAI. We will focus on this in Chap. 3. The topological order parameters are still applicable, with the momenta in the Green's functions replaced by twist boundary conditions [71].

1.3.3 General Theory for Topological Insulator

There are two general theories to describe the topological insulators. (1) Topological band theory based on Z_2 topological band invariant of single particle states [45, 72, 60, 46, 47]. This theory is valid only for noninteracting systems. However, it is simple to evaluate which band insulators are topologically nontrivial and has attracted much attention. The starting point is energy band. For integer-class topological insulator (e.g., quantum Hall effect), the knowledge of Bloch states over the whole Brillouin zone is needed to get the Chern number because of the lack of time reversal symmetry. For time reversal invariant Z_2 topological insulator, the information over the entire Brillouin zone is not needed to calculate topological order Z_2 . Only a few high-symmetry points are enough to determine the topological class for systems with inversion symmetry [60]. (2) Topological field theory [48]. It is generally valid for interacting and disordered systems where energy band cannot be obtained. The topological field theory can reduce exactly to the topological band theory in the noninteracting limit [65].

1.4 Organization

In Chap. 2, biased bilayer and trilayer graphene with disorder distributed only in bottom layer is studied. We calculate the conductance of two opposite bias voltage and give a detail research on the conductance ratio under different conditions. We also explain the fascinating results by full band model Hamiltonian. This work gives a new direction of field effective transistor based on graphene.

In Chap. 3, we study the disordered topological Anderson insulator in a 2D geometry. The phase diagram of finite systems is reported and evolution of phase boundaries with very large system size is also studied. We report conductance distributions near several phase transitions and compare them with critical conductance distributions for well-known models.

Summary of our work is given in Chap. 4.

CHAPTER 2

DISORDER INDUCED FIELD EFFECT TRANSISTOR IN BILAYER AND TRILAYER GRAPHENE

2.1 Introduction

Bilayer graphene has recently attracted considerable research interest [31, 18, 73]. One of the most remarkable properties of bilayer graphene is the ability to open an energy gap and control its size in the spectrum by a perpendicular bias voltage. This property has been shown experimentally [74, 32, 75] and theoretically [76, 77, 78]. It indicates that graphene-based switchable devices can be realized, such as field effect transistor (FET). Typically, to perform the ‘on’/‘off’ digital logic, a finite gap is required for the ‘off’ state. Many experimental work have focused on using the bias voltage to induce a high current ratio [75, 79, 73, 80]. The improvement of the ‘on’-‘off’ current ratio is mainly based on the reduction of the ‘off’ current.

Another configuration drawing researchers’ attention is trilayer graphene. This material’s energy dispersion and electron transport properties are sensitive to the sheet stacking sequence [81, 82, 33, 83, 84, 85]. The low energy dispersion of ABA stacked trilayer graphene [86, 87] is a combination of linear and quadratic terms. A perpendicular bias voltage changes the band overlap, but does not open a gap. In contrast, the energy dispersion of ABC stacked trilayer graphene is almost cubic [87, 88], and a bias voltage can open and tune a band gap. Dual gated ABC stacked trilayer graphene [89, 90] has been reported to exhibit a large ratio between the on current and the off current. The current ratio in ABA stacked trilayer graphene [91] is much lower because there is no band gap in this stacking.

Disorder is also a focus in the previous studies of graphene. Impurities in substrate are inevitably produced during the nanofabrication processes. Interaction with the substrate produces a disorder potential which affects the graphene lattice. The picture that disorder in the substrate translates into disorder in the graphene sheet via charge transfer has been confirmed by experiments [22, 92]. The factors causing on-site energy changes are simulated as Anderson disorders. On the other hand, structural distortion may be induced in graphene due to its lattice mismatch with the substrate [93]. Moreover, varying bonds can be formed between graphene and different terminations of the substrate [94, 95, 96]. The lattice mismatch and binding of graphene with the substrate are considered as bond disorders in this work. The existence of the substrate can change the properties of the graphene deposited on it by doping [21], opening a gap at the Dirac cone [95] and shifting Fermi level [97]. To get rid of the effect from the substrate, some research groups have done much effort to fabricate suspended monolayer [98], bilayer [99, 100] and trilayer [101] graphenes. However, obtaining free standing graphene remains a complicated process.

In this proposal, the influence of substrate plays a positive role in enhancing ‘on’-‘off’ current ratio by weakening the ‘off’ signal. As the interaction between two adjacent layers of multilayer graphene is weak, the effect of the substrate is considered on bottom layer only. We employ tight-binding model to calculate the longitudinal transports of bilayer and trilayer graphene under opposite perpendicular bias voltages for different disorder strengths. When opposite perpendicular bias voltages are applied, the transport electrons concentrate either in top or bottom graphene layer accordingly [78]. The electrons concentrating in the bottom layer are affected by substrate dramatically, therefore the corresponding longitudinal transport will be restrained obviously. If the electrons concentrate in the top layer, the longitudinal transport is not affected considerably. Considering the previous two electron transport behaviors under opposite bias voltages, we define the conductance ratio as ‘ G_{+U}/G_{-U} ’ to

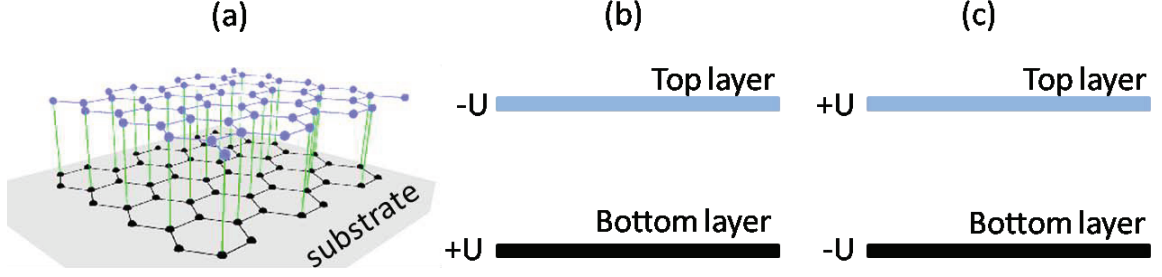


Figure 2.1: (a) Schematic diagram of bilayer graphene supported by a substrate. (b) Voltage $+U$ is applied to the bottom layer while $-U$ to the top layer. (c) Voltage $-U$ is applied to the bottom layer while $+U$ to the top layer. The black coloring in figures (b) and (c) represents disorder caused by the bottom layer's coupling to the substrate

characterize the 'on'-'off' ratio, where U is always a positive value. G_{+U} is the conductance when bias voltage - $+U$ to the bottom layer and $-U$ to the top layer - is applied, while the conductance G_{-U} corresponds to the inverse bias voltage. Similar to Giant magnetoresistance (GMR) [102] effect, where the resistance is controlled by the magnetic field, in this model, the resistance (the current) can be governed by the voltage.

We begin in Sec. II by describing the model and methods. In Sec. III.A, The effect of bond and Anderson disorders on zigzag/armchair edged bilayer graphene is discussed. In Sec. III.B, we use the effective four band low-energy description to interpret the conductance ratio of bilayer graphene. In Sec. III.C, ABA and ABC stacked trilayer graphene are investigated. Finally, the conclusion is given in Sec. IV.

2.2 Model

The system of interest is schemed in Fig. 2.1a. In our theoretical model, the effect of substrate is depicted by disorder. Two kinds of disorders are taken into account: Anderson disorder and bond disorder. Four kinds of structures are studied in our

work, i.e., zigzag and armchair edged AB stacked bilayer graphenes, zigzag edged ABA and ABC stacked trilayer graphenes. Voltage $+U$ ($-U$) is applied to the bottom layer (top layer) of multilayer graphene as shown in Fig. 2.1b. The inverse voltage - $-U$ to the bottom layer, $+U$ to the top layer - is applied as shown in Fig. 2.1c. The black (dark) color represents disorder in the bottom layer. The tight-binding Hamiltonian for biased AB stacked bilayer graphene, ABA and ABC stacked trilayer graphenes [103, 104, 105] are

$$\begin{aligned}
H_{AB} = & -t \sum_{\langle i,j \rangle; L=B,T} \left(a_{i,L}^\dagger b_{j,L} + h.c. \right) \\
& + \sum_{i; L=B,T; c=a,b} U_L c_{i,L}^\dagger c_{i,L} \\
& -t_\perp \sum_i \left(b_{i,T}^\dagger a_{i,B} + h.c. \right)
\end{aligned}$$

$$\begin{aligned}
H_{ABA} = & -t \sum_{\langle i,j \rangle; L=B,M,T} \left(a_{i,L}^\dagger b_{j,L} + h.c. \right) \\
& + \sum_{i; L=B,T; c=a,b} U_L c_{i,L}^\dagger c_{i,L} \\
& -t_\perp \sum_i \left(b_{i,T}^\dagger a_{i,M} + a_{i,M}^\dagger b_{i,B} + h.c. \right)
\end{aligned}$$

$$\begin{aligned}
H_{ABC} = & -t \sum_{\langle i,j \rangle; L=B,M,T} \left(a_{i,L}^\dagger b_{j,L} + h.c. \right) \\
& + \sum_{i; L=B,T; c=a,b} U_L c_{i,L}^\dagger c_{i,L} \\
& -t_\perp \sum_i \left(b_{i,T}^\dagger a_{i,M} + b_{i,M}^\dagger a_{i,B} + h.c. \right)
\end{aligned}$$

Here, a_i (b_i) is the annihilation operator on sublattice A (B) for electrons on site i . ‘B’, ‘M’, ‘T’ represent the bottom, middle and top layers respectively. $\langle \dots \rangle$ denotes the nearest neighbors. The intralayer nearest hopping term $t = 2.7eV$ is taken as the energy unit. The interlayer hopping $t_\perp = 0.1496t$ couples two neighboring layers in a Bernal stacking pattern. Interlayer voltage difference $2U$ is given by setting

$U_T = -U_B = +U$ or $U_T = -U_B = -U$. For trilayer graphene, no voltage is applied to the middle layer. In bottom layer, nonmagnetic on-site disorder or bond disorder is randomly distributed in the interval $[-W/2, W/2]$, where W is the disorder strength. The multilayer graphene is centered, adjoining two opposite semi-infinite leads [106]. The two leads are free from disorder and modeled by pristine graphene ribbons. The same Fermi energy is set in the leads as in the central region. Nonequilibrium Green's function based on tight-binding model [107, 106, 108] is employed to calculate the conductance in the longitudinal direction. The leads used to probe the inplane conductance are accounted as self-energy. For all calculations, the width of the central area of interest is about $149a$ and the length is about $344a$, where $a = 0.142nm$ is the nearest neighbor distance. In the presence of disorder, the conductance is averaged over 200 random configurations at fixed disorder strength, Fermi energy and perpendicular bias voltage.

2.3 Results and Discussion

2.3.1 Electron Transport in Bilayer Graphene

In this section, we will show how we calculate the conductance ratio. The effect of disorder strength, disorder types, voltage magnitude and edge types are studied.

Fig. 2.2 illustrates the conductance and conductance ratio of zigzag edged bilayer graphene at voltage $U = 0.03t$. Different line colors (line styles) correspond to different disorder strengths as labeled in Fig. 2.2f. The bias voltage applied in Fig. 2.2a and 2.2d corresponds to that shown in Fig. 2.1b, while voltage in Fig. 2.2b and 2.2e corresponds to that shown in Fig. 2.1c. Fig. 2.2c (Fig. 2.2f) is the ratio of the conductances in Fig. 2.2a and Fig. 2.2b (Fig. 2.2d and Fig. 2.2e).

The effect of Anderson disorder is shown in the upper panels. Fig. 2.2a displays the conductance as a function of Fermi energy. Clear plateaus are observed at disorder strength being zero. When the disorder strength deviates from zero, the conductance

approaches to zero in the vicinity of the Dirac point and the quantized plateaus vanish. The larger the disorder strength, the greater the deviation from the quantized conductance plateaus is. When the perpendicular bias voltage is inverted, the corresponding conductance is shown in Fig. 2.2b. The quantized conductance plateaus are the same as those in Fig. 2.2a when the disorder strength is zero. With the increase of disorder strength, near the Dirac point the conductance does not decrease as fast as that in Fig. 2.2a. In particular, the conductance plateau is destroyed by Anderson disorder more easily when the Fermi energy is away from the Dirac point in Fig. 2.2b. Fig. 2.2c shows the ratio of conductance obtained from applying opposite bias voltages, namely, G_{+U}/G_{-U} . There is a dip smaller than 1 at Fermi energy near the Dirac point. With the increase of disorder strength, the maximum value of the conductance ratio gets larger and a broad peak appears.

The case of bond disorder is shown in the lower panels. In Fig. 2.2d and 2.2e, the conductance is not suppressed by disorder greatly near the Dirac point. Away from the Dirac point, the conductance plateaus are destroyed more easily by bond disorder in Fig. 2.2e. The conductance ratio for bond disorder is shown in Fig. 2.2f. No dip is observed. The peak of conductance ratio locating at $E \approx U$ is obvious at large disorder strength.

Fig. 2.2 shows clearly the effect of Anderson and bond disorder on conductance and conductance ratio. To get a higher conductance ratio, a larger disorder strength is preferred and bond disorder is more efficient. For both Anderson and bond disorder, the conductance ratios tend towards a constant value 1 when the Fermi energy is far from the Dirac point.

The effect of bias voltage on the conductance ratio is shown in Fig. 2.3. The conductance ratio is shown as a function of Fermi energy at specific disorder strengths $W = 0.5t$ (left panels) and $W = 1.2t$ (right panels). Different colors (line styles) represent the bias voltages applied - $0.05t$, $0.08t$, $0.12t$ and $0.2t$ - as labeled in Fig. 2.3d.

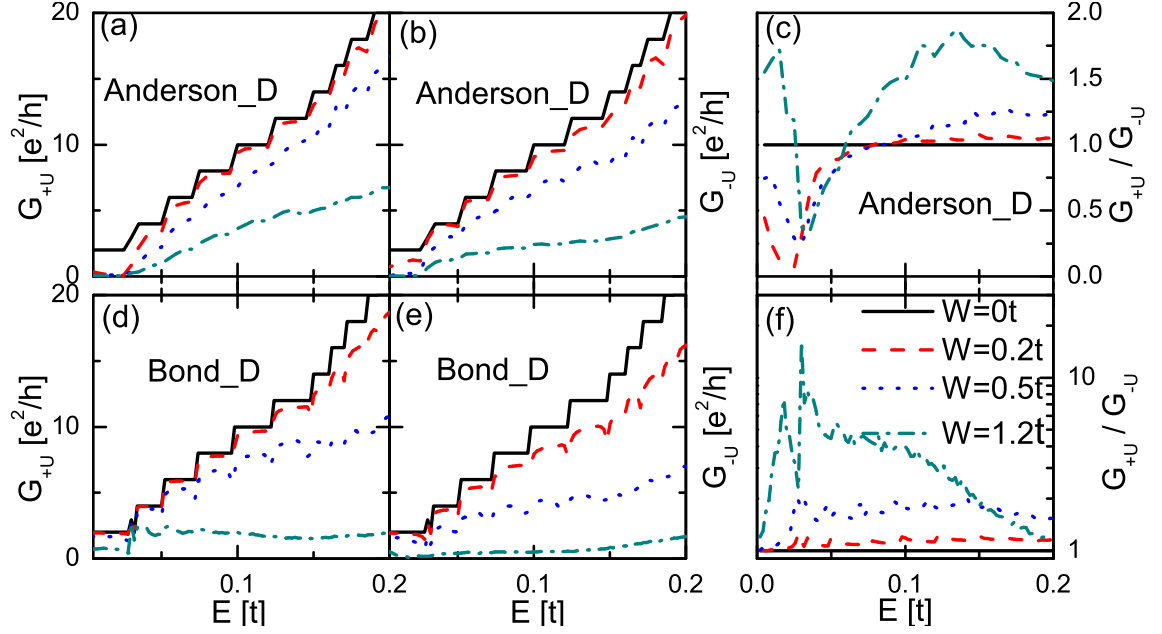


Figure 2.2: Conductance and relative conductance ratio (G_{+U}/G_{-U}) of zigzag edged bilayer graphene as a function of Fermi energy. The effect of Anderson (bond) disorder is shown in the upper (lower) panels. (a) and (d) are the conductances G_{+U} when voltage $+U$ ($-U$) is applied to bottom (top) layer (as the bias voltage applied in Fig. 2.1b). (b) and (e) are the conductances G_{-U} when voltage $-U$ ($+U$) is applied to the bottom (top) layer (as the bias voltage applied in Fig. 2.1c). The parameter $U = 0.03t$. (c) and (f) are the ratio of the conductances obtained from the above two opposite voltages. Different colors (line types) represent different disorder strengths as labeled in (f).

The vertical dashed lines $U1$, $U2$, $U3$ and $U4$ represent the cases where the Fermi energy equals to $0.05t$, $0.08t$, $0.12t$ and $0.2t$ respectively.

Anderson disorder is displayed in the upper panels. In Fig. 2.3a, where disorder W is fixed at $0.5t$, the conductance ratio shows a dip smaller than 1 in the vicinity of the Dirac point and increases rapidly at $E = U$. The maximum value of conductance ratio gets larger with the increase of the bias voltage. The conductance ratio at $W = 1.2t$ in Fig. 2.3b shows similar behavior as $W = 0.5t$ in Fig. 2.3a. However, the raise of conductance ratio at $E = U$ is more significant, where pronounced peaks are observed.

Fig. 2.3c and Fig. 2.3d show the conductance ratio in the case of bond disorder. Lines $U1$, $U2$, $U3$, and $U4$ compare bond disorder to Anderson disorder. We find that in both cases the conductance ratio increases when $E = U$. The peaks are very clear and high. Especially in Fig. 2.3d, where $W = 1.2t$, the maximum of G_{+U}/G_{-U} is about 120. The large conductance ratio is desirable for making effective FET as long as the ‘on’ signal is large enough to be detected in experiment. When the disorder $W = 1.5$, conductance ratio can be as large as 700 (not shown in the figure). In fact, the absolute conductance is large enough compared with the detectable value in experiment [79]. When $U = 0.2t$, $W = 1.5t$, the conductance at the peak is about $20e^2/h$ in the case of ‘on’ and about $0.03e^2/h$ in the case of ‘off’. In Xia’s experiment results [79], we convert the experiment current to conductance in unit of e^2/h . The maximum conductance is about $26e^2/h$ while the minimum is about $0.26e^2/h$ at room temperature and $0.026e^2/h$ at 20K.

From Fig. 2.3, we conclude that large bias voltage facilitate high conductance ratio. Bond disorder is favorable for large G_{+U}/G_{-U} . For all of the four cases, the conductance ratios tend towards 1 when the Fermi energy is far from the Dirac point.

Armchair edged bilayer graphene is characterized in Fig. 2.4 to make a comparison with zigzag edges. Only the bond disorder - the more efficient one to get large conduc-

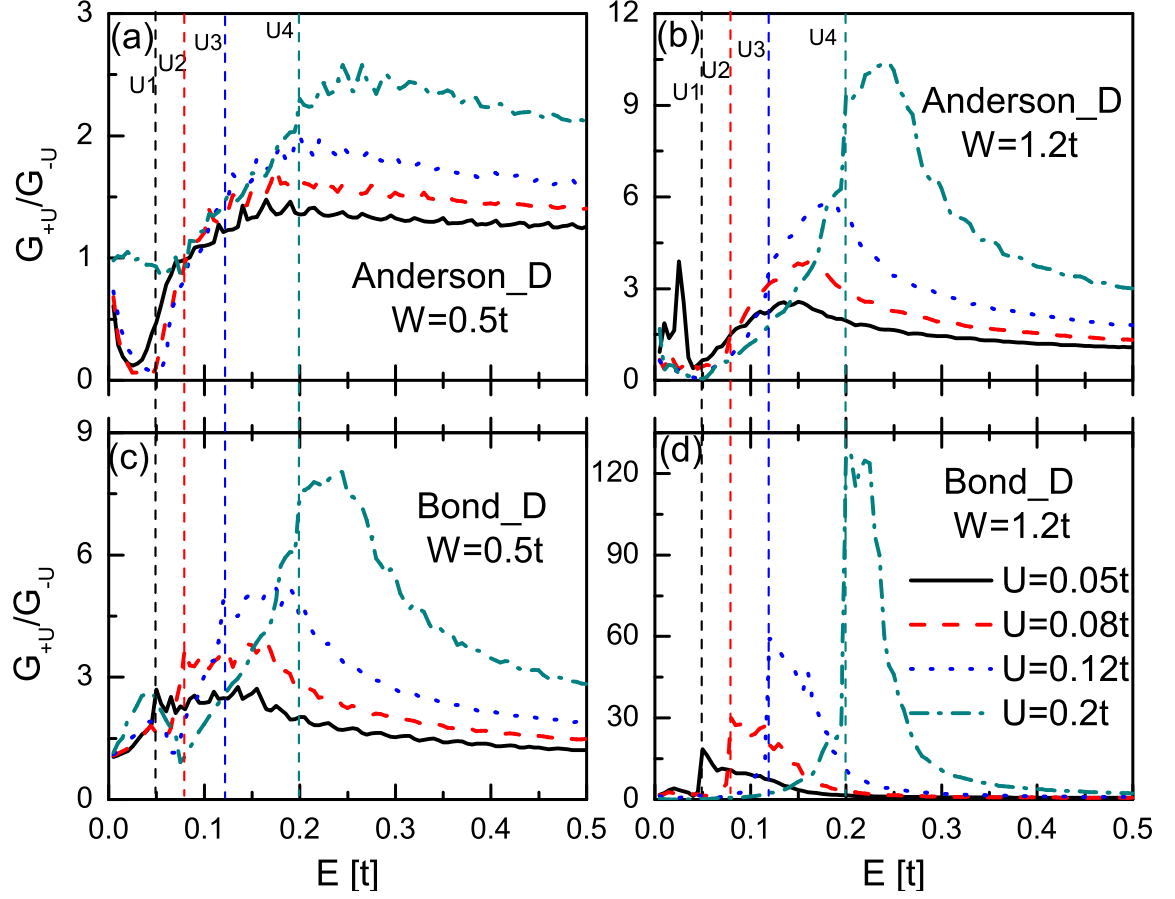


Figure 2.3: Conductance ratio (G_{+U}/G_{-U}) of zigzag bilayer graphene as a function of Fermi energy. The effect of asymmetric Anderson (bond) disorder is shown in the up (lower) panels. The disorder strength W is $0.5t$ in (a) and (c), $1.2t$ in (b) and (d). Different colors (line types) represent different bias voltages U as labeled in (d). The vertical dashed lines $U1$, $U2$, $U3$ and $U4$ are guide lines corresponding to the condition $E = U$, which are $0.05t$, $0.08t$, $0.12t$, and $0.2t$ respectively.

tance ratio - is considered. Fig. 2.4a-d give the results of G_{+U}/G_{-U} when bias voltages $U = 0.03t$, $U = 0.08t$, $U = 0.12t$ and $U = 0.2t$ are applied respectively. The inset of Fig. 2.4d shows the conductance at $U = 0.2t$. It is shown that the conductance is almost zero when the Fermi energy is small (lying inside the gap). As the conductance is negligible, there is no need to calculate the ratio of the conductances. Therefore, G_{+U}/G_{-U} is truncated inside the gap. The four critical Fermi energies indicating the gaps are $0.0279t$, $0.0547t$, $0.0635t$ and $0.0701t$ for different applied voltages $0.03t$, $0.08t$, $0.12t$ and $0.2t$ respectively. Different line colors (line styles) indicate different disorder strengths as labeled in Fig. 2.4c. The larger the disorder, the higher the peak of conductance ratio is. By comparing the highest peaks in Fig. 2.4a-c, we can find that the conductance ratio increases with the bias voltage. Similar to the case of zigzag edged bilayer graphene, the peaks of G_{+U}/G_{-U} appear also at $E = U$. The maximum value of G_{+U}/G_{-U} in armchair edged bilayer graphene is comparable with that in zigzag edged bilayer graphene. The similar behavior indicates that edge types are not important in this new proposed FET.

In this section, we studied the effect of disorder types, disorder strength, bias voltage magnitude and the edge type of bilayer graphene nano-ribbon on the conductance ratio. It is found that bilayer graphene with large bond disorder strength under high bias voltage shows the highest conductance ratio. What also impresses us is that the conductance ratio peak always appears at $E = U$. We will explain this behavior in the next section.

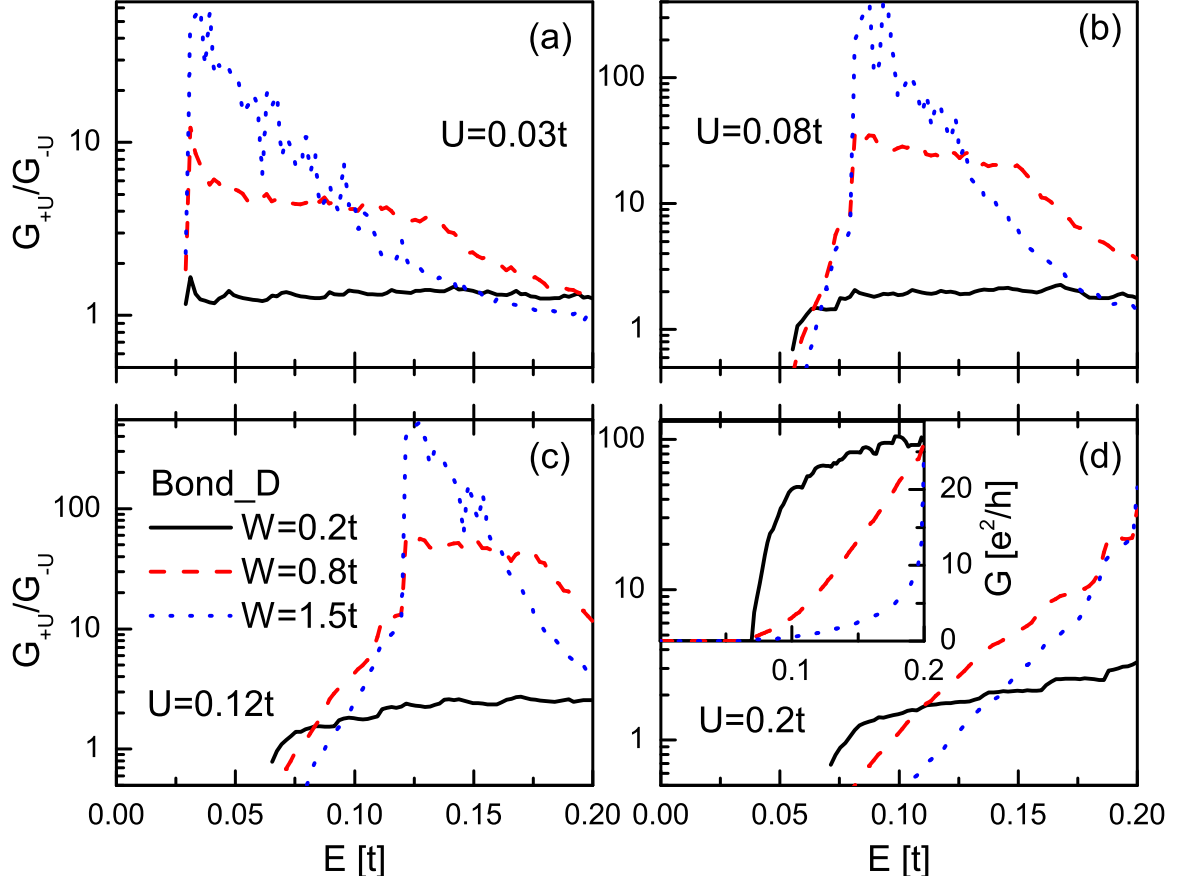


Figure 2.4: Conductance ratio (G_{+U}/G_{-U}) of armchair bilayer graphene. Different bias voltages are applied: (a) $U = 0.03t$, (b) $U = 0.08t$, (c) $U = 0.12t$ and (d) $U = 0.2t$. The conductance ratio is truncated inside the gap, i.e., smaller than the Fermi energy $0.0279t$, $0.0547t$, $0.0635t$ and $0.0701t$ for different applied voltages $0.03t$, $0.08t$, $0.12t$ and $0.2t$ respectively (referring to the dispersion in Fig. 2.5). The different line colors (line types) indicate different disorder strengths as labeled in (c). The inset in (d) gives the conductances for different disorder strengths at $U = 0.2t$.

2.3.2 Four Band Model for Bilayer Graphene

Four band low energy model is employed to explain the conductance behavior in bilayer graphene. The Hamiltonian for bilayer graphene [87, 105] around \vec{K} point is

$$H_{AB} = \begin{pmatrix} U & v_F k_- & 0 & 0 \\ v_F k_+ & U & t_\perp & 0 \\ 0 & t_\perp & -U & v_F k_- \\ 0 & 0 & v_F k_+ & -U \end{pmatrix}$$

where $v_F = \frac{3a}{2\hbar}t$ is the Fermi velocity, and $k_\pm = k_x \pm ik_y$. Following this equation, we calculate the dispersion and local electron distribution (LED) in each layer shown in Fig. 2.5.

The dispersion of bilayer graphene is shown in Fig. 2.5a-d at bias voltages $0.03t$, $0.08t$, $0.12t$, $0.2t$ respectively. For low applied voltages (Fig. 2.5a), the bands are fairly flat near the Fermi energy. When the voltage gets larger (Fig. 2.5b), the gap opened by the voltage gets larger and the so called ‘Mexican hats’ [87] exist. The crowns of the ‘Mexican hats’ are just at the points $E = +U$ and $E = -U$ respectively. The minimum value of the gap between the conduction and valence band [76], locating at $k \neq 0$, is $\Delta' = \frac{2Ut_\perp}{(4U^2 + t_\perp^2)^{1/2}}$. For huge asymmetry $U \gg t_\perp$ (as in Fig. 2.5d), the gap saturates at $\Delta' \approx t_\perp$ while for modest asymmetry $U \ll t_\perp$ (as in Fig. 2.5a), $\Delta' \approx 2U$. In Fig. 2.5d, the signal ‘+’/‘-’ means the energy bands moving up/down with the applied voltage.

Fig. 2.5e-h show the LED corresponding to the dispersion in Fig. 2.5a-d. Each energy band can be traced back to either the top or the bottom graphene layer roughly since the interlayer coupling is weak. The relationship between the dispersion and LED is focused at $U = 0.2t$. A gap between $E \approx \pm 0.07t$ in Fig. 2.5d corresponds to the LED being 0 for both layers in Fig. 2.5h. When the Fermi energy moves up to the ‘Mexican hat’, where $E = \Delta'$, the bands associated with bottom and top layers coexist. LED of the layer applied $+U$ voltage is slightly larger than that of the

other layer. For bias voltage applied in Fig. 2.1b, the electrons concentrate on the bottom layer. Since disorder is only in bottom layer, the conductance is destroyed more easily. When the bias voltage is inverted, as shown in Fig. 2.1c, the LED is also inverted. In this case, the conductance is not affected by the disorder that much since the electrons concentrate in the top layer. As a result, G_{+U}/G_{-U} is smaller than 1 in the region within the ‘Mexican hat’. When the Fermi energy moves up to the critical point $E = U$, only the energy band moving down retains in the dispersion relation. Therefore, in Fig. 2.5h, the LED increases rapidly at $E = U$ in the layer applied $+U$ voltage. When the bias voltage is applied as in Fig. 2.1b, the conductance is not affected significantly. When the bias voltage is inverted as shown in Fig. 2.1c, the conductance is reduced greatly. Therefore, the conductance ratio show maximum from $E = U$ to the existence of the second band (we call this region ‘H’ for convenience, as show in Fig. 2.5). This picture gives a good explanation for the rapid increase of G_{+U}/G_{-U} at $E = U$ in Fig. 2.3 and Fig. 2.4.

The dependance of the conductance ratio on the disorder strength and bias voltage magnitude can also be explained by Fig. 2.5. The large disorder strength plays more important roles in weakening the electron transport in bottom layer. In region ‘H’, the ratio of LEDs in bottom and top layers is high, so the larger the disorder, the more prominent effect on conductance ratio is. When the magnitude of the bias voltage gets larger, the region ‘H’ becomes narrower and the ratio of LEDs in the two layers becomes higher. This can be seen clearly by comparing the LEDs in the region ‘H’ in Fig. 2.5e-h. Because of the high ratio of LEDs in the two layers, the effects of disorder on the conductance contrast a lot when opposite bias voltages applied. As a result, G_{+U}/G_{-U} will show sharp and high peaks in region ‘H’.

The tending towards 1 of the conductance ratios when the Fermi energy is far from the Dirac point can also be explained. When the Fermi energy is far from the Dirac point, the LEDs of the bottom and top layers are equal to each other. Therefore,

disorder has the same effect on the conductances of opposite bias voltages. As a result, the conductance ratio goes to 1.

This model can explain the behavior that conductance ratio is smaller than 1 near the Dirac point in Fig. 2.3 qualitatively, while the critical Fermi energies are not consistent with each other very well. One reason is that nano-ribbons are employed to calculate the conductance while this model Hamiltonian is for infinite system. Another reason is that the change of the spectrum due to the disorder can be considered as the shift of Fermi energy relatively [97]. The LEDs of the top and bottom layers do not deviate from each other greatly in the existing of 'Mexican hat'. The difference becomes significant in the region 'H'. Near the Dirac point, the renormalized Fermi energy is possible to fall inside the energy region with large LED because of the disorder. The large LED dominates the behavior of the conductance ratio. Therefore, the conductance ratio is not always smaller than one when $|E| < U$.

2.3.3 Trilayer Graphene with two Different Stacking Orders

Before moving to the characterization of electron transport in trilayer graphene, we investigate the LED for both ABA and ABC stacked graphenes in every layer to capture the rough physics. Similar to bilayer graphene, six band low energy model is adopted. The Hamiltonian for trilayer graphene with two kinds of stacking orders [87, 105] around \vec{K} point are

$$H_{ABA} = \begin{pmatrix} U & v_F k_- & 0 & 0 & 0 & 0 \\ v_F k_+ & U & t_\perp & 0 & 0 & 0 \\ 0 & t_\perp & 0 & v_F k_- & 0 & t_\perp \\ 0 & 0 & v_F k_+ & 0 & 0 & 0 \\ 0 & 0 & 0 & 0 & -U & v_F k_- \\ 0 & 0 & t_\perp & 0 & v_F k_+ & -U \end{pmatrix}$$

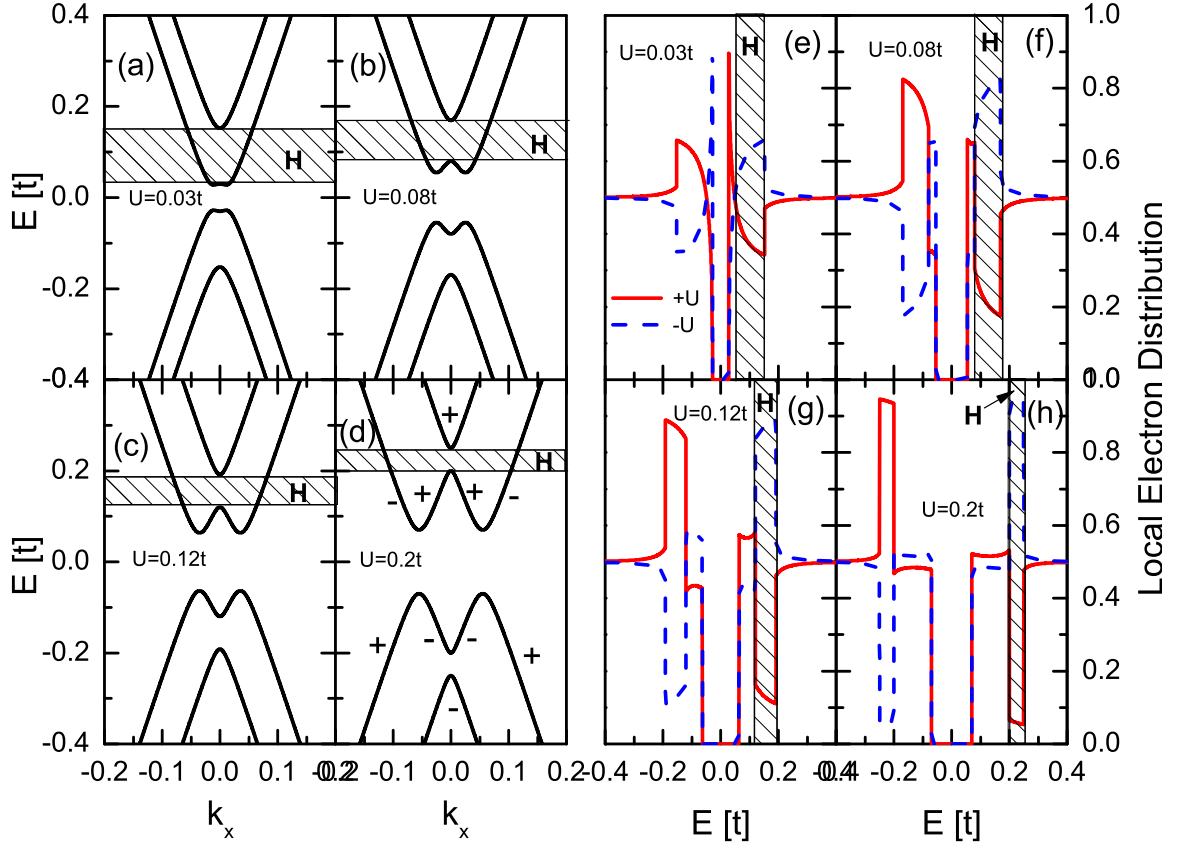


Figure 2.5: Dispersion and LED of bilayer graphene. Different bias voltages are applied: (a) $U = 0.03t$, (b) $U = 0.08t$, (c) $U = 0.12t$ and (d) $U = 0.2t$. The signs '+' and '-' in (d) indicate the direction of the bands moving with the voltage. (e)-(h) show the LED corresponding to the dispersion in (a)-(d). The red solid and blue dashed lines indicate the LED in layers applied voltage $+U$ and $-U$ respectively. The shaped region 'H' indicate the existence of a single band.

$$H_{ABC} = \begin{pmatrix} U & v_F k_- & 0 & 0 & 0 & 0 \\ v_F k_+ & U & t_\perp & 0 & 0 & 0 \\ 0 & t_\perp & 0 & v_F k_- & 0 & 0 \\ 0 & 0 & v_F k_+ & 0 & t_\perp & 0 \\ 0 & 0 & 0 & t_\perp & -U & v_F k_- \\ 0 & 0 & 0 & 0 & v_F k_+ & -U \end{pmatrix}$$

The same parameters as in bilayer graphene are employed. Using these Hamiltonian, we can get the eigenvalues and eigenfunctions, from which the LED in every layer is calculated. Fig. 2.6e-h give the LED corresponding to the dispersion relations in Fig. 2.6a-d. Similar dispersion relations are obtained in former researches [81, 82, 33]. For ABA stacking, the dispersion is a combination of linear and quadratic dispersion without perpendicular voltage. The perpendicular bias voltage breaks the mirror reflection symmetry with respect to the central layer, leading to the hybridization of the linear and parabolic low-energy bands. Since the degeneracy is not totally destroyed, no gap is opened, as shown in Fig. 2.6a and 2.6c. For ABC stacking, the perpendicular bias voltage lifts the degeneracy of two-fold cubic dispersion, leading to a gap, as shown in Fig. 2.6b and 2.6d. The two horizontal critical lines a1 and a2 in Fig. 2.6a (the same as in Fig. 2.6b, 2.6c and 2.6d) define the region where only one single band moving down exists. In this region, LED in the layer applied negative voltage $-U$ is much larger than that in the layer applied voltage $+U$. This is confirmed in Fig. 2.6e-h indicated by the black vertical dashed lines. The LED of trilayer graphene becomes more complicated than that of bilayer graphene. What stands out is that the LED in the layer applied $-U$ voltage (blue dotted line) is much larger than that in the layer applied $+U$ voltage (red solid line) in the Fermi energy interval of the following regions: lines a1 to a2 in Fig. 2.6e (2.6a), b1 to b2 in Fig. 2.6f (2.6b), c1 to c2 in Fig. 2.6g (2.6c) and d1 to d2 in Fig. 2.6h (2.6d). Following the discussion for bilayer graphene, we can deduce that the conductance ratio will show

peaks in those energy regions.

Fig. 2.7 shows the conductance ratio for zigzag edged ABA and ABC stacked trilayer graphenes. Different line colors (line styles) represent different bond disorder strengths ($W = 0.2t, 0.8t$ and $1.5t$). The larger the disorder strength, the higher the G_{+U}/G_{-U} is. As expected, the conductance ratios show large values at the Fermi energies between lines a1 and a2 in Fig. 2.7a, b1 and b2 in Fig. 2.7b, c1 and c2 in Fig. 2.7c, d1 and d2 in Fig. 2.7d. The effects of voltage magnitude on the conductance ratio of trilayer graphene are similar to that of bilayer graphene, i.e., G_{+U}/G_{-U} increases with the bias voltage.

What impresses us is that the magnitudes of conductance ratios in ABA and ABC stacked trilayer graphenes are comparable even though no gap exists in ABA stacked trilayer graphene. This is extremely important. It is a common idea that a finite gap is required for the ‘off’ signal to get a high ‘on’-‘off’ ratio [80, 79]. In the present proposal, the ‘on’ and ‘off’ signals come from the relative transport when opposite bias voltages are applied to multilayer graphene in the existing of disorder only in the bottom layer. The ratio does not depend on the gap, even though gap exists in the bilayer graphene and ABC stacked trilayer graphene under the perpendicular bias voltage.

2.4 Conclusion

A new proposal of FET taking advantage of disorder in multilayer graphene is presented. The main contributions of our paper are that (1) a disordered bottom layer can dramatically increase the conductance ratio, and (2) a high conductance ratio can be obtained even when there is no bulk band gap. The asymmetry between the bottom and top layers from perpendicular bias voltage and disorder distributed only in the bottom layer play important roles. The effect of disorder strengths and disorder types on transport of bilayer/trilayer graphene is studied under different bias

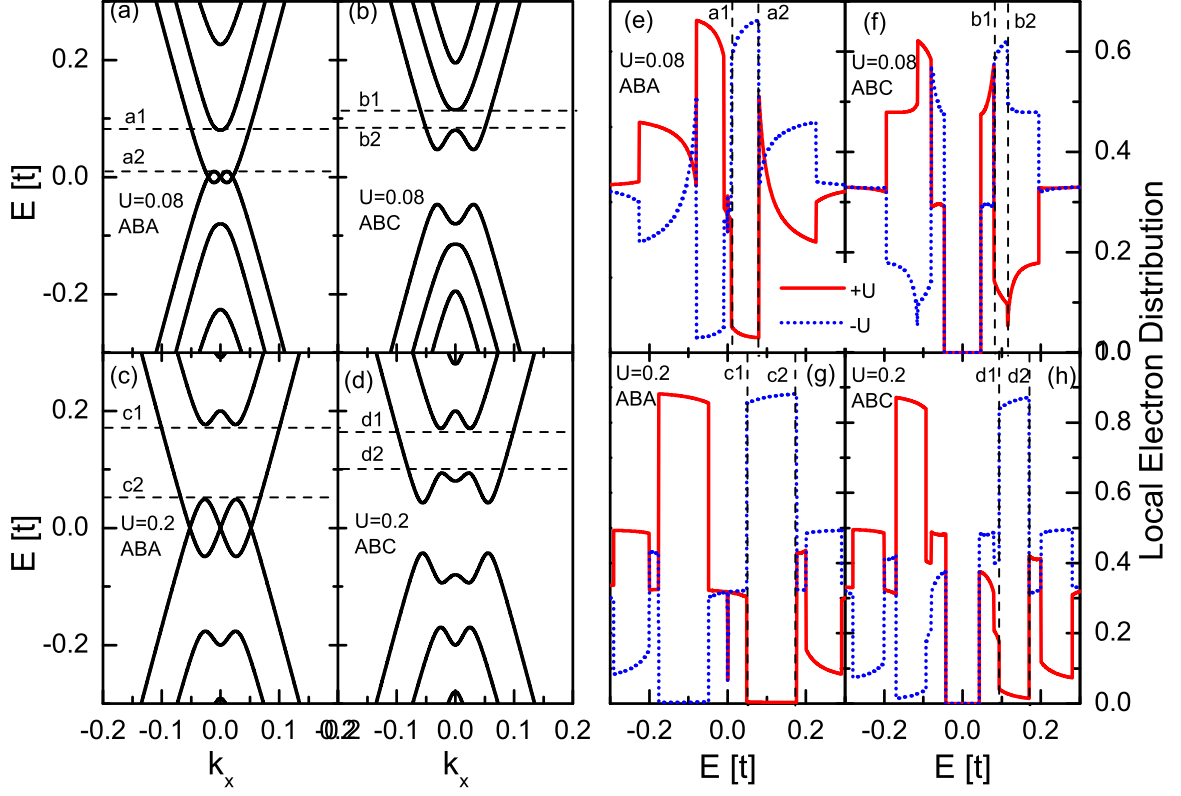


Figure 2.6: Dispersion and LED of trilayer graphene. Bias voltages $U = 0.08t$ (upper panels) and $U = 0.2t$ (lower panels) are applied. (a) and (c) show the energy dispersion for ABA stacking. (b) and (d) show the dispersion for ABC stacking. The black horizontal dashed lines represent the critical changes of energy bands. (e)-(h) give the LED in the layer applied voltage $-U$ (blue dot lines) or $+U$ (red solid lines). The black vertical dashed lines in (e)-(h) give the same Fermi energies as the black horizontal dashed lines indicated in (a)-(d).

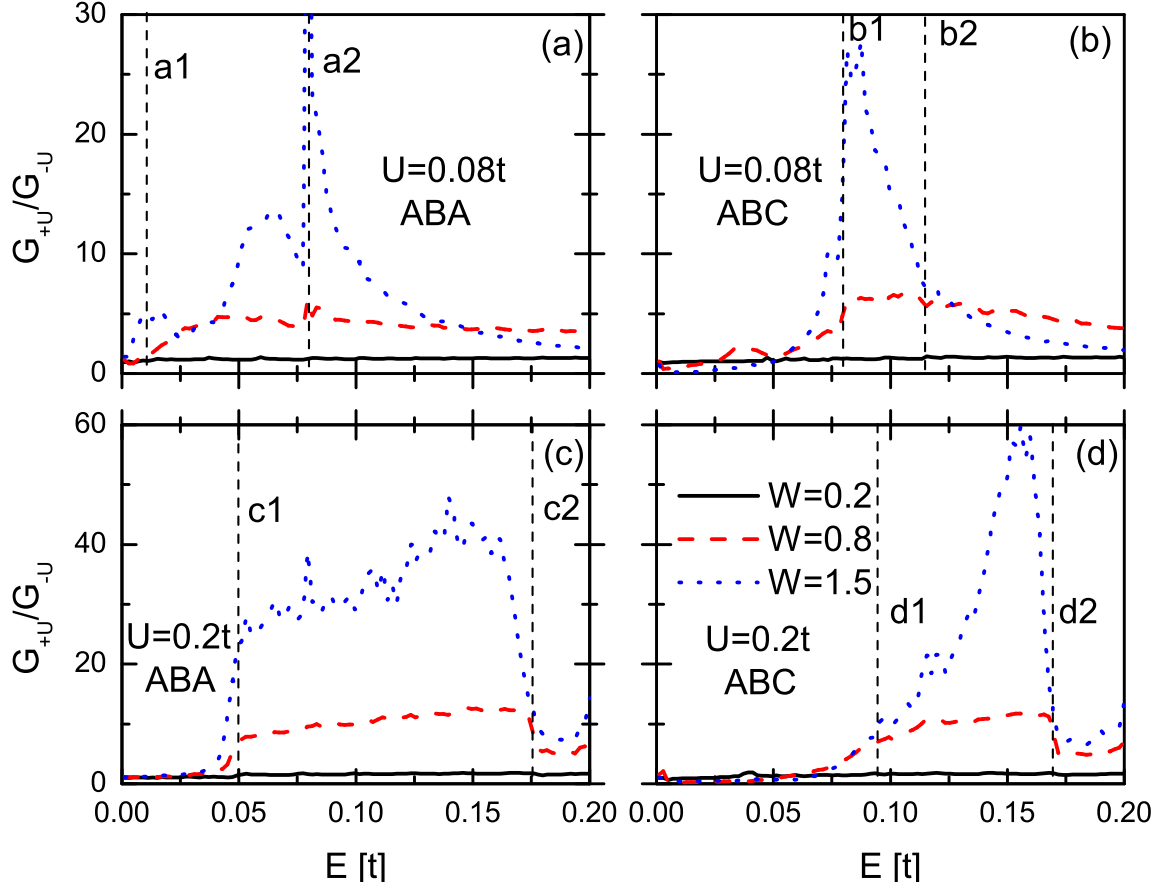


Figure 2.7: Conductance ratio of zigzag edged ABA (left panels) and ABC (right panels) stacked trilayer graphenes. Different bias voltages are applied: $U = 0.08t$ in (a) and (b), $U = 0.2t$ in (c) and (d). The different line colors (line types) indicate different disorder strengths. The black vertical dashed lines correspond to the same critical Fermi energies as shown in Fig. 2.6.

voltages. The conductance ratio becomes higher with the increase of the disorder strength for both Anderson and bond disorders. Large applied bias voltage is favorable to get high conductance ratio at fixed disorder strength. Importantly, the ‘on’ conductance is large enough to be detected while the ‘off’ signal can be suppressed efficiently by disorder. Therefore, disorder plays a positive role in enhancing ‘on’-‘off’ ratio in this kind of FET by weakening the ‘off’ signal. As a result, disorder induced by substrate is no longer a shortcoming and intended doping in bottom graphene layer is beneficial. The conductance ratio is well explained by the full band Hamiltonian. The study on ABA stacked trilayer graphene shows that gap is not essential for the large conductance ratio, i.e., an energy gap is not necessary for this proposed FET.

CHAPTER 3

PHASE STRUCTURE OF THE TOPOLOGICAL ANDERSON INSULATOR

3.1 Introduction

Topological insulators [60, 61, 109, 110, 111, 112] are the focus of considerable interest for their quantized edge conductance which is similar to that seen in the integer quantum Hall (IQH) effect. Unlike IQH systems, TIs require neither magnetic fields nor low temperatures. TIs exhibit a gap in the spectrum of bulk states, and bridging that gap is a band of edge states; if the Fermi energy is within the gap then electrons flow only along the edge and not in the bulk. In two dimensions there are only two edge states, and they are helical, which means that they have opposite spins and opposite momenta. If spin is conserved then backscattering is prohibited and the edge conductance is quantized. Therefore the bulk band gap coincides with a plateau of quantized conductance. All these properties are consequences of bulk band inversion in a system with time-reversal (T) symmetry, and are topologically protected against small perturbations which are T -symmetric, such as weak non-magnetic disorder.

Li et al [66] studied the Bernevig-Hughes-Zhang (BHZ) Hamiltonian [51] which models the 2-D topological insulator $HgTe$, but they tuned the mass parameter to a positive value ($M = 1$ meV) so that there is no inversion of bulk bands, no band of edge states, and no topological physics. Li et al. introduced non-magnetic disorder and found a region of quantized conductance at intermediate disorder strengths, which implies the existence of conducting edge states. Since their $M = 1$ meV model has no edge states at zero disorder, they believed that the observed edge states are not

caused by the band inversion which is central to topological insulators. Moreover, Li et al. believed that the quantized region occurs in a region where the bulk states are localized, not in a band gap like topological insulators. They dubbed the observed quantized region a ‘topological Anderson insulator phase’.

Soon afterward Groth et al [67] published a paper titled ‘Theory of the Topological Anderson Insulator’ which argued that the topological Anderson insulator can be explained by mass inversion, the same as the zero-disorder topological insulator. They used the Coherent Potential approximation (CPA, or SCBA) [113, 114] to calculate an effective Hamiltonian which includes some disorder effects. Renormalized strengths of the mass term and Fermi level can be extracted from the effective Hamiltonian. Strong enough disorder changes the sign of the mass term, producing a band inversion and topologically protected edge states. Yamakage et al [69] and Prodan [68] have performed numerical calculations of the evolution of the TAI conductance plateau when both the mass and the disorder strength are varied separately. They studied cases which were intermediate between an ordinary TI (negative mass, no disorder) and a TAI (positive mass, finite disorder), and showed that the TI conductance plateau changes continuously into the TAI conductance plateau. This numerical evidence indicates that the TAI conductance plateau is caused by inversion of the bulk bands.

Groth et al [67] argued that the weak-disorder boundary of the conductance plateau is a crossing from the bulk band into a band gap, and is not an Anderson transition. This implies that the absence of bulk conductance near this boundary is due to an absence of bulk states rather than their localization. Groth et al also gave numerical evidence that the weak-disorder boundary of the conductance plateau matches well to the CPA’s prediction of the bulk band edge, and that the conductance plateau is accompanied by a bulk band gap. All of these findings were qualified by a proviso restricting their validity to ‘small systems accessible to numerical calculations’

[67].

Recently Chen et al [115] and Zhang et al [70] have found evidence that the TAI conductance plateau is populated by bulk states. Moreover, Guo et al [116] and Chen et al [115] plotted the region where the CPA predicts a bulk gap, and demonstrated that this region is much smaller than the conductance plateau which has been determined numerically. Outside the gapped region Chen et al [115] found numerical evidence that robust edge states coexist with bulk states, and they also reported a metallic phase lying between the quantized and insulating phases. These results reveal ongoing questions about the precise nature of the TAI conductance plateau and about the overall phase diagram.

In disordered systems there are two important length scales: the scattering length, and the localization length which is typically much longer. The scattering length scale regulates the density of states, while the localization length scale regulates conduction and localization. The CPA correctly includes scattering physics but discards the quantum interference processes which determine the localization length scale. Although the CPA does correctly predict the density of states because this quantity is controlled at leading order by scattering physics, it is unable to predict the conductivity of systems that are bigger than the localization length. This was already obvious in the original TAI papers, which show a quantized-to-insulator transition at large disorder that is not predicted by the CPA. The TAI phase diagram could change substantially in the infinite volume limit.

In this light it is important to note that all studies of the TAI have been limited to small system sizes. Studies of the conductance have minimized the computational time by examining pseudo-one-dimensional rectangular strips. Two dimensional geometries have only one length scale ($L_x = L_y$), while pseudo-one-dimensional geometries have one extra length scale (both L_x and L_y). This complicates the phase diagram, producing an insulating phase along the weak-disorder edge of the conduc-

tance plateau. This phase is only one of many finite size effects which blur and distort the phase diagram. In a strip with short dimension L_x and long dimension L_y , the finite size effects are determined by L_x . The maximum value of L_x until now has been $L_x = 300a$, in a paper which used $L_x = 130a$ data to determine the TAI phase diagram (Ref. [115]). Other studies have considered $L_x = 12a$ (Ref. [70]), $L_x = 64a$ (Ref. [69]), $L_x = 50a$ (Ref. [68]), and $L_x = 150a$ (Ref. [66]). While these lengths are sufficient to measure scattering physics, in much of the phase diagram they are unable to probe the localization length scale. Moreover finite size effects are quite large, blur the phase boundaries, and prevent a precise understanding of individual phases.

In section 3.2 of this paper we obtain a clear picture of the physics at length scales $L_x = L_y \leq 280a$. This brings the scattering length scale into sharp focus, and allows us to see clearly both a scaling region where the conductance plateau is accompanied by a bulk gap and a larger scaling region where the plateau persists without an accompanying bulk gap. (We use the term ‘scaling region’ rather than ‘phase’ only because this black and white gapped vs. ungapped dichotomy must be refined a bit in larger systems.) We use the two-dimensional $L_x = L_y$ geometry, and we change the system size by a factor of four ($L = 70, 140, 280a$) to get a clear picture of finite size effects. The central result of this section is the TAI phase diagram, Figure 3.3. We also discuss the eigenstates in the conductance plateau: both their peculiar property of growing rather than shrinking when the disorder strength is increased, and their fractality.

In section 3.3 we turn our focus toward the localization length scale and increase the system size to $L = 1120a$. The phase boundaries become more clearly defined, and allow us to rule out the existence of extra phases at the edges of the TAI conductance plateau. At the same time the phase boundaries move because localization effects are becoming important. We also find that the bulk band gap is invaded by

localized bulk states. The density of bulk states in the gap is exponentially small as is typical for Lifshitz tails, which allows the gapped and ungapped scaling regions to be distinguished from each other. Lastly we report the conductance distributions on various phase boundaries and compare them with known critical distributions for the integer quantum Hall and quantum spin Hall systems.

3.1.1 The TAI Model

Following the original TAI paper [66], we study the BHZ tight binding model [117] of 2-D topological insulators. The mass can be tuned by changing the sample thickness, and we choose a positive mass $M = 1$ meV so that there is no band inversion and no edge states at zero disorder. The BHZ model's momentum representation is:

$$\mathcal{H} = \begin{bmatrix} h(\vec{k}) & 0 \\ 0 & h^*(-\vec{k}) \end{bmatrix}$$

with

$$\begin{aligned} h(\vec{k}) = & (A/a)\sigma_x \sin(k_x a) + (A/a)\sigma_y \sin(k_y a) + M\sigma_z \\ & + 2(\sigma_z B/a^2 + I D/a^2)(2 - \cos(k_x a) - \cos(k_y a)) \end{aligned}$$

where, $D = 512 \text{ meV nm}^2$, $B = 686 \text{ meV nm}^2$, $A = 364.5 \text{ meV nm}$, $a = 5 \text{ nm}$, $M = 1 \text{ meV}$. The basis has four orbitals: the first two are s and p orbitals with spin $s_z = 1/2$, and the last two are s and p orbitals with spin $s_z = -1/2$. $\sigma_{x,y,z}$ are the Pauli matrices. The Hamiltonian conserves the s_z component of the spin, which is protected by the combination of inversion symmetry and axial symmetry around the growth axis. This symmetry can be broken by a quantum well or gate electrode [69], and also can be broken by disorder. We follow the original TAI papers [66, 112, 67] which preserved the s_z symmetry and introduced nonmagnetic on-site disorder randomly distributed in the interval $[-W/2, W/2]$, where W is the disorder strength. With this disorder the BHZ model factorizes into two independent 2×2 Hamiltonians

which are time-reversal counterparts of each other. Therefore all of our calculations of the conductance, eigenvectors, and eigenvalues concern themselves only with the $s_z = 1/2$ sector, which is governed by a 2×2 Hamiltonian. The conductances and densities of states which we report are exactly $1/2$ of the correct values that are obtained when all four orbitals are included.

It is very important to recognize that the BHZ model's s_z symmetry substantially changes its localization physics [67, 68, 118, 119]. If kinetic or disorder terms which break the s_z symmetry are added to the BHZ model, then factorization is disallowed and one must use the original 4×4 model which belongs to the symplectic symmetry class and can exhibit metallic phases [69]. In contrast, the factorized 2×2 model belongs to the unitary symmetry class, the same as systems exhibiting the integer quantum Hall effect. Unlike symplectic models, unitary models are always localized in infinite 2-D systems.

The principal focus of this paper is on the TAI phase diagram in a two-dimensional $L_x = L_y$ geometry. This question is most clear in an isolated sample without any leads, where it can be studied by analyzing eigenstates and eigenvalues. With the exception of our conductance data, all of our numerical results come from the leads-free geometry. However for the conductance we use leads with width $W = L_x = L_y$ adjoining two opposite sides of the the disordered sample. As discussed in section 3.2.3, the introduction of leads does not change the phase diagram significantly. We evaluate the conductance using the Caroli formula[120, 121] $G = -\frac{e^2}{h} \text{Tr}((\Sigma_L^r - \Sigma_L^a)G_{LR}^r(\Sigma_R^r - \Sigma_R^a)G_{RL}^a)$, where G^a, G^r are the advanced and retarded Green's functions connecting the left and right leads and $\Sigma_{L,R}$ are the self-energies of the leads. We evaluate the lead self-energies using the well-known iterative technique developed by Lopez Sancho et al [122]. Following References [112] and [67], we use semi-infinite leads that are described by the BHZ Hamiltonian and are free from disorder. Because the mass $M = 1$ meV is positive, in the leads the bulk band gap does not contain any edge

states. Therefore all conducting channels in the leads are bulk channels, and the leads do not conduct when the Fermi energy is in the gap $|E_F| < M$. Errors associated with the leads will be discussed in Appendix 3.4.

3.2 The Phase Diagram in Systems of Size $L \leq 280a$

In this section we will defer the question of the infinite size limit and focus instead on the physics and phases in finite systems with $L \leq 280a$. First we will show that the TAI conductance plateau contains both a gapped and an ungapped scaling region, and will show that the CPA gives a good description of the gapped scaling region but not the ungapped scaling region. The centerpiece of this section is the phase diagram, which shows all the phases and their boundaries. Lastly we will study the spatial structure of the bulk states.

Because our Hamiltonian belongs to the unitary ensemble, we expect that in the infinite volume limit all bulk states are localized and non-conducting. Nonetheless for systems of size $L \leq 280a$ a large portion of the phase diagram exhibits an average conductance that is proportional to the system size L for all $L \leq 280a$, implying that the bulk states are extended and conducting even at $L = 280a$. We will call this behavior ‘bulk conduction’.

3.2.1 The TAI Conductance Plateau

Figure 3.1a demonstrates TAI conductance quantization, which is manifested as a plateau in the average conductance $\langle G \rangle = 1$ with boundaries at the disorder strengths $W1 \approx 105$ meV and $W3 \approx 334$ meV. The Fermi energy is kept fixed at $E = 12$ meV in this figure. The large-disorder edge at $w3$ is a transition from quantized conductance to the localized phase. As is typical of second-order phase transitions, it is broadened at finite system sizes, narrowing the TAI conductance plateau. When the system size is increased from $L = 50a$ to $L = 200a$ the transition narrows, and therefore $\langle G \rangle$

increases towards one on the left of $W3$ and decreases towards zero on the right. This produces a crossing point that allows us to estimate the position of the true phase transition in an infinite system. In this limit the conductance transition at $W3$ is a step function which changes directly from one to zero. In other words, at $W3$ the conducting edge states are abruptly destroyed in a process analogous to the integer quantum Hall effect.

The small disorder edge at $W1$ is a transition from bulk conduction to quantized conductance. Here the conductance exhibits a meeting point, and the rise to the left of that meeting point becomes more and more abrupt as the system size is increased. The trend is toward a very sharp conductance transition at $W1$ that moves directly from bulk conduction to $\langle G \rangle = 1$.

In Figure 3.1b we calculate eigenstates, and show their scaled average distance¹ from the edge, $\langle d/L \rangle = L^{-1} \int d\vec{x} |\psi(\vec{x})|^2 d(\vec{x})$. Between ≈ 108 meV and $W2 \approx 129$ meV this observable converges toward zero as the system size is increased from $L = 50a$ to $L = 200a$, indicating that the eigenstates are edge states. However outside of this range $\langle d/L \rangle$ is independent of the system size, indicating that the eigenstates are bulk eigenstates, distributed in the interior of the sample.

We conclude that the TAI conductance plateau is composed of two scaling regions, one with a bulk band gap, and the other without. In the TAI-I region to the left of $W2$ the bulk gap leaves only edge states, which are responsible for conduction. However there is a second TAI-II region to the right of $W2$ with both bulk states and edge states; it has no bulk gap. Since the number of bulk states scales with L^2 while the number of edge states scales with L , the bulk states dominate $\langle d/L \rangle$. The bulk states are localized, maintaining the TAI conductance quantization $\langle G \rangle = 1$. Figure 3.1c's plot of the average local density of states $\langle \rho \rangle$ confirms this picture: in the TAI-

¹We calculate the distance of \vec{x} from each of the four edges. $d(\vec{x})$ is the minimum of these four distances.

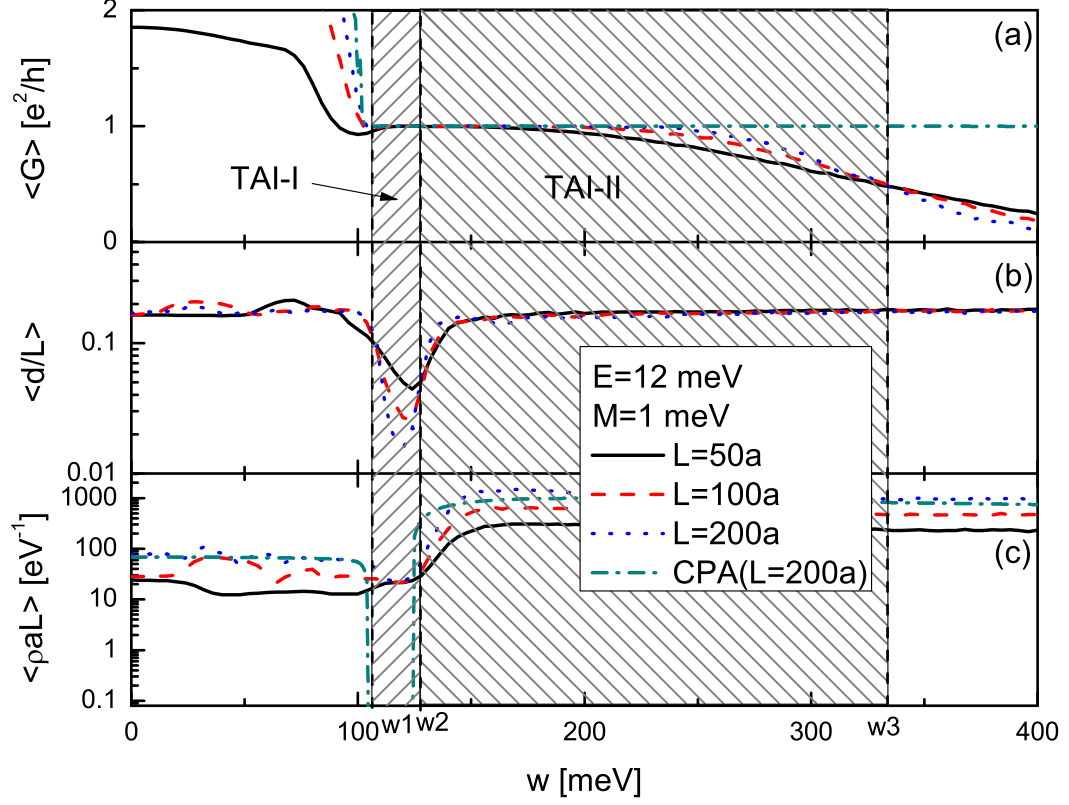


Figure 3.1: Two TAI scaling regions: TAI-I with only edge states, and TAI-II with both edge states and localized conducting states. Lines $W1$ and $W3$ mark the edges of the TAI conductance plateau, and $W2$ marks the boundary between the gapped TAI-I scaling region on the left and the ungapped TAI-II scaling region on the right. Panes a, b, and c show respectively the conductance, the scaled distance from the edge, and $L a$ times the local density of states. The CPA ($L = 200a$) lines report the results of the coherent potential approximation. The Fermi energy is fixed at $E = 12$ meV.

I (gapped) region $\langle \rho L \rangle$ is independent of the system size L , as is expected of edge states. In the TAI-II (ungapped) region $\langle \rho L \rangle$ is proportional to L , indicating that bulk states are far more numerous than edge states.

A bulk band gap is not necessary for TAI conductance quantization. Figure 3.2a displays the conductance at a fairly large value of disorder, $W = 200$ meV. The boundaries of the TAI conductance plateau coincide with the clear crossing points at $E1 \approx -8$ meV and $E2 \approx 50$ meV. Figure 3.2b shows that the local density of states ρ is independent of the system size, implying that there is no bulk band gap. The entire TAI conductance plateau lies in the TAI-II scaling region, which is characterized by the coexistence of conducting edge states with localized bulk states. This shows that a mobility gap - even in the absence of a band gap - is sufficient for producing TAI conductance quantization.

Figure 3.2 crosses the weak-disorder boundary of the TAI conductance plateau at line $E2$, but this crossing is not accompanied by a bulk band edge. This establishes that the weak-disorder boundary is accompanied by a bulk band edge only in the gapped TAI-I region, not in the ungapped TAI-II region. In the TAI-II region the bulk states exhibit an Anderson transition as the weak-disorder boundary is crossed, and localization is responsible for preventing bulk conduction. In section 3.3.3 we will show that in the TAI-I gap there is an exponentially small density of localized bulk states; the TAI-I weak-disorder boundary is marked by an Anderson transition from bulk conduction to localized bulk states. Zhang et al [70] found these localized bulk states in very small $8a \times 8a$ systems. Their localization is responsible for the TAI conductance plateau where only edge states conduct. In section 3.3.1 we will study systems as large as $1120a \times 1120a$ and find that the weak-disorder boundary of the conductance plateau is always accompanied by a mobility edge, both in the gapped TAI-I region and in the TAI-II region where there is no gap and no bulk band edge.

The gapped TAI-I scaling region and its boundary with the ungapped TAI-II

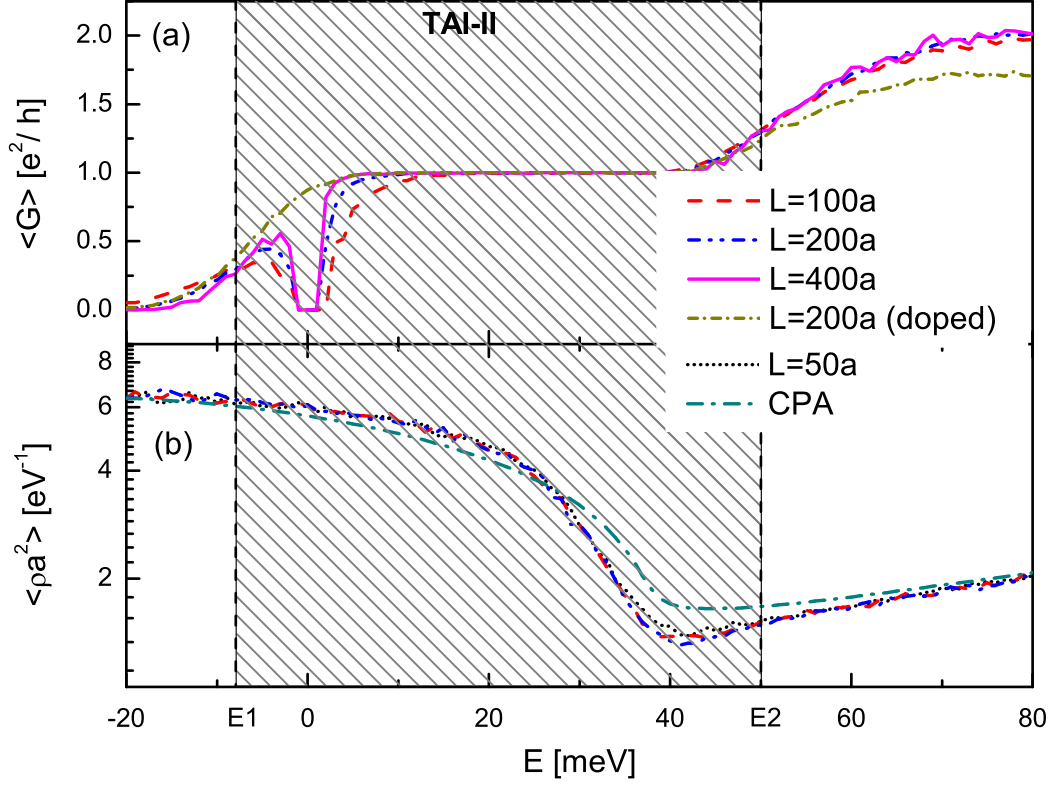


Figure 3.2: TAI Conductance Quantization without a Band Gap. The disorder strength is fixed at $W = 200$ meV. $E1$ and $E2$ label crossing points which mark the edges of the conductance plateau. The local density of states ρ is independent of system size L , indicating that it is dominated by bulk states. The conductance gap near $E = 0$ is caused by the disorder-free leads, which do not conduct at $|E| \leq 1$ meV. The ‘ $L=200a(\text{doped})$ ’ line shows clearly that when the leads are doped to $E = 25$ meV the conductance plateau extends to the $E1$ crossing point.

scaling region can be understood entirely within the coherent potential approximation [113, 114]. Figure 3.1c and Figure 3.2b include the CPA density of states ρ , which provides excellent predictions of the true density of states everywhere except in the gapped TAI-I region. The CPA is a mean field approximation that does not include edge physics, so inside the TAI-I region it predicts only the gap $\rho = 0$ and not the edge states. The CPA density of states nonetheless makes a spectacularly good prediction of all boundaries of the TAI-I region, including its boundary with the neighboring TAI-II region.

At an intermediate step in calculating the CPA density of states one obtains the self-consistent mean-field Hamiltonian H_{CPA} , whose real part can be interpreted as a renormalized band gap and renormalized Fermi level. The Fermi level's position (inside or outside the gap) can predict the weak-disorder boundary of the TAI conductance plateau [67]. This predictor duplicates the CPA density of states' success with the gapped TAI-I region's weak-disorder boundaries, but unlike the DOS it does not find the boundary with the TAI-II region.

Our picture of two scaling regions distinguished by bulk vs. edge scaling is based on analysis of data at finite system sizes $L = 50, 100, 200a$. It matches very well with the CPA, which incorporates only physics at the scattering length scale, and neglects physics at the much longer length scale of localization. We conclude that the gapped TAI-I region and its boundary with the ungapped TAI-II region is caused entirely by short-distance scattering physics. Our picture of the two regions will require some refinement when the system size is increased, as will be discussed in section 3.3, but scattering physics and the bulk band gap will still strongly influence the phase diagram.

The Coherent Potential Approximation Hamiltonian

We have re-used the self-consistent mean-field Hamiltonian H_{CPA} in a recursive Green's function calculation of the conductance, omitting the imaginary part of H_{CPA} which is anti-Hermitian and which destroys the CPA's predictive power at almost all values of the disorder strength W . The CPA conductance, calculated while omitting the imaginary part of H_{CPA} , is shown in Figure 3.1a. It is correct at disorder strengths smaller than $W3$, including the TAI-I region where there are only edge states. However, the CPA conductance fails to predict the localization of the edge states at $W3$, and remains quantized even at very large disorder. In addition, the CPA Hamiltonian H_{CPA} does not predict the localized bulk states seen in the ungapped TAI-II region and does not distinguish the TAI-I and TAI-II regions; it predicts that both the density of states ρ and $\langle d/L \rangle$ retain edge values at all disorders larger than $W1$. In summary, the mean-field Hamiltonian H_{CPA} correctly predicts observables both in the bulk conducting phase and in the gapped TAI-I region, but fails to predict the localized bulk states seen in the TAI-II region and in the ungapped insulating phase, and also fails to find the large-disorder edge of the TAI conductance plateau.

3.2.2 Phase Diagram

The phase diagram is reported in Figure 3.3. Each data point represents a crossing point or meeting point which was determined by comparing observables at three different system sizes as described in our discussion of Figures 3.1 and 3.2. Numerical errors will be discussed in Appendix 3.4. The triangles along line $g3$ were obtained from crossing points of the scaled distance from the edge $\langle d/L \rangle$, and all other data points were obtained from the average conductance $\langle G \rangle$. The open boxes report crossing points observed on vertical lines keeping W fixed, while the filled data points were determined on horizontal lines keeping E fixed.

We have connected the data points with lines. Lines $eg1$, $g1$, $g2$, and $eg3$ repre-

sent a bulk conduction-to-quantized transition which separates the TAI plateau from Region-I A and Region-I B. In Region-I A the conductance scales with system size L , signifying bulk conduction. Region-I B also exhibits bulk conduction, and is separated from the insulating (zero conductance) Region-II by an Anderson transition. Line $eg2$ represents a quantized-to-insulator transition, and separates the localized phase in Region-II from the conductance plateau. Contrary to Chen et al [115], we see no evidence of an intervening metallic phase along $eg2$; we will discuss this further in section 3.3.2. We have not done a careful analysis of the phase diagram above $E = 60$ meV, but we have found that at $E = 100$ meV there is no conductance plateau. This suggests that lines $eg1$ and $eg2$ meet and merge into an Anderson transition somewhere between $E = 60$ meV and $E = 100$ meV. Line $g3$ separates the gapped TAI-I region from the ungapped TAI-II region, which is marked by hatched lines.

Our phase diagram includes also the CPA predictions for the phase structure. Both the area with blue shading and the small area between dashed at lines at $W < 35$ meV are characterized by a bulk band gap, as calculated ² using the CPA. The CPA bulk band gap succeeds brilliantly in predicting the boundaries of the gapped TAI-I region (shaded blue): its predictions agree with the data points on lines $g1$, $g2$, and $g3$ to within 2 meV. This allows us to estimate the positions of two tricritical points at the ends of line $g3$: they lie at $(W \approx 101, E \approx 2)$ meV and at $(W \approx 158, E \approx 25)$ meV.

We mark the gap closure and rebirth at $W \approx 35$ meV with line m . To the left of line m the material is not in a topological phase, because the mass $M = 1$ meV is positive. To the right of line m a bulk band inversion begins and a topologically protected band of edge states appears and persists until $W \approx 370$ meV. At $W \approx 370$ meV the edge band collapses, the bulk band inversion terminates, and the material is no longer a topological insulator.

²We determined the boundaries of the shaded region by comparing the CPA Local DOS to 10^{-8} .

Line $eg3$ separating the bulk conducting phase in Region-I B from the quantized TAI-II region is merely a guide to the eye; our data do not allow us to decide exactly where the bulk conducting phase terminates. Along the $W = 100$ meV line we see an interval with bulk conduction sandwiched between the quantized TAI-I region and the insulating phase, while at $W = 105, 110$ meV this evidence disappears quickly. This small portion of the phase diagram is extremely complex, with four phases and regions and two tricritical points near each other. Analysis is complicated even further by the leads, which if left undoped display very large finite size effects near the $E = 0$ meV axis.

Line $eg2$ marks the lower boundary of the band of edge states. It seems unlikely that this boundary follows the edge of the conductance plateau along $eg3$ and $g2$, since this would involve a discontinuous transition between the $eg2$ line which runs along $E \approx -8$ meV and $g2$ line at $E = 2$ meV. More likely the band of edge states extends into the bulk conducting Region-I B but its contribution to the conductance is hidden by the bulk conduction signal. Similarly, the upper boundary of the edge band may extend into Region-I A, above lines $g1$ and $eg1$. We conjecture that the lower boundary of the edge band may interpolate smoothly between line $eg2$ and the point where the bulk band gap closes and reopens.

$b1$ and $b2$ mark lines where the Fermi level passes through the edges of the bulk band gap - using a Fermi level and band gap that have been derived from the self-consistent mean-field CPA Hamiltonian. These predictors fail to predict the TAI-II portion of the weak-disorder boundary of the TAI plateau. For instance, line $b1$ predicts that the $W = 200$ meV line exits the TAI conductance plateau at $E = 38$ meV. Referring to figure 3.2, we find that although there is minimum in the local density of states at $E = 41$ meV, the true phase boundary (a crossing point in the conductivity) is located at $E = 50$ meV. Lines $b1$ and $b2$ do not seem to be good predictors of the ungapped TAI-II region's boundaries.

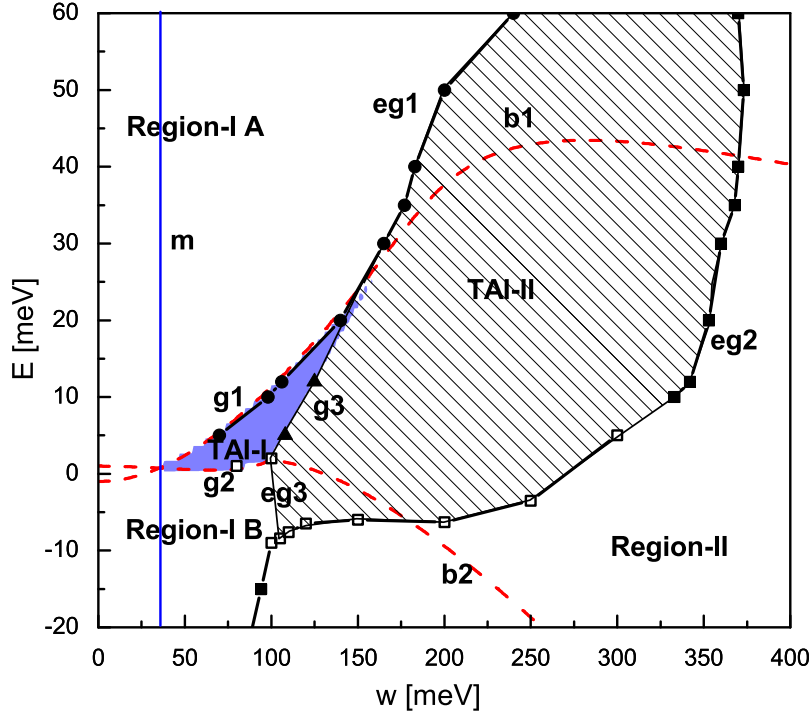


Figure 3.3: The TAI phase diagram at mass $M = 1$ meV. In Regions I A and I B the bulk states conduct. An Anderson transition separates Region I B from Region II, where the system is insulating. The TAI conductance plateau includes both the gapped TAI-I region (colored blue) and the ungapped TAI-II region (hatched lines.) The region inside the dashed lines to the left of line m is gapped and has no surface states. This phase diagram reflects only physics at length scales $L \leq 280a$.

3.2.3 Bulk State Delocalization and Fractality

Remarkably, eigenstates grow when the disorder strength is increased throughout a large portion of the ungapped TAI-II region. This is the reverse of most systems: usually when the disorder strength is increased eigenstates shrink and move toward localization. We calculated eigenstates of the TAI hamiltonian and measured the participation ratio (PR) $PR^{-1} = \int d^2\vec{x} |\psi(x)|^4$, which is a measure of the eigenstate volume. The PR ranges from one for a fully localized eigenstate to the system volume V for a fully extended eigenstate. The lower right inset of Figure 3.4 reports the average PR, which includes contributions from both bulk and edge states. Near the transition from bulk to quantized conductance the average PR drops precipitously to very small values around $40a^2$, indicating that the eigenstates become very localized. This region of hyperlocalization is very small: it adjoins a broad peak that rises through the TAI-II region, reaches a maximum near the quantized-insulator transition, and falls in the insulating phase. In other words the eigenstates steadily grow with increasing disorder, reach their maximum size near the quantized-insulator transition, and then begin to localize again. The width of the peak decreases as the system size is increased.

Lines $b1$ and $b2$ show where the mean-field Fermi level passes through the edges of the mean-field bulk band gap. Figure 3.4 compares these lines to a contour of the average PR at $\langle PR \rangle = e^5 a^2 \approx 148a^2$. Earlier we found that the transition from bulk to quantized conduction is predicted by $b1$ and $b2$ only near the gapped TAI-I region; $b1$ and $b2$ fail at the edge of the ungapped TAI-II region. Now we find that the hyperlocalized region (labeled PR) is predicted well by line $b1$ even in the TAI-II region. In Figure 3.4 we include both edge and bulk states in $\langle PR \rangle$, so in the gapped TAI-I region we see values typical of delocalized edge states, much larger than $148a^2$. We have calculated the average PR of only the bulk states, omitting edge states, and have found that the bulk states are hyperlocalized throughout the entire TAI-I

region, with a minimum $\langle PR \rangle$ of about $10a^2$. In summary, lines $b1$ and $b2$ seem to be good predictors of the bulk hyperlocalized region but not of the phase transition to the TAI-II region.

The upper right inset of Figure 3.4 shows the fractal dimension d_2 , which is the derivative of $\ln\langle PR \rangle$ with respect to the logarithm of the system size L ; we report $d_2(400a, 200a) = (\ln\langle PR(L = 400a) \rangle - \ln\langle PR(L = 200a) \rangle) / \ln 2$, $d_2(200a, 100a)$, and $d_2(100a, 50a)$. Non-integer values indicate fractal states. Regarding non-fractal states, the integers $d_2 = 2$, 1 , and 0 respectively indicate conducting extended bulk states, edge states, and localized states. Figure 3.4 shows that throughout the TAI-II region the bulk eigenstates are fractals. Since their size is a power of the system volume, they are sensitive to the boundary conditions. It is remarkable that the average conductance $\langle G \rangle$ remains quantized, indicating that these bulk states do not conduct even though they are edge-sensitive.

Like the participation ration $\langle PR \rangle$, the fractal exponent d_2 forms a broad peak centered near the quantized-localized phase transition, and the peak width decreases as the system size is increased. Along the $E = 12$ meV line we find that the peaks in both d_2 and $\langle PR \rangle$ are located near $W = 290$ meV and don't move much as the system size is increased. This disagrees with our conductance data, which indicates that the quantized-insulator phase transition is located at $W > 300$ meV. This discrepancy could be evidence for a systematic disagreement between data based on the conductance (obtained with infinite leads) and data based on diagonalization of the Hamiltonian (obtained with no leads). However it seems more likely that the discrepancy is a finite size effect: we will see in section 3.3.2 that the conductance crossing point shifts from $W \approx 380$ meV to $W \approx 320$ meV as the system size is increased from $L = 50a$ to $L = 400a$. Most likely the peaks in both d_2 and $\langle PR \rangle$ coincide with the quantized-localized phase transition.

Groth et al [67] measured the scaling exponent $\nu = 2.66 \pm 0.15$ at the quantized-

insulator phase transition, which is compatible with the known value[123] of 2.59 for the integer quantum Hall effect; they suggested that the TAI quantized-insulator transition belongs the IQH universality class. Here we report that the maximum value of the fractal exponent $max(d_2)$ near the quantized-insulator phase transition is approximately $d_2 \approx 1.5$, and is consistent with the value of 1.5 ± 0.1 seen in previous studies of the fractal exponent at the integer quantum Hall transition [124, 125, 126, 127].

3.3 Infinite Volume Limit

In the previous section we confined ourselves to system sizes $L \leq 280a$, and obtained a phase diagram appropriate to that length scale. This brought the scattering physics into sharp focus, but finite size effects blurred and shifted the phase boundaries. In disordered systems the physics at the localization length scale can be quite different from the physics at smaller length scales. In 2-D systems the localization length scale can be extremely large. Therefore it is very important to attempt some extrapolation of the phase diagram to larger system sizes.

Already the $280a \times 280a$ systems of the previous section compare well to previous TAI studies, but in the present section we calculate certain observables in systems that are four times bigger, multiplying the computational time by 256. We were able to do this for several reasons. Firstly, fluctuations in G drop to zero at the transition from bulk conduction into the TAI conductance plateau, so in this region we need only very small data sets. Secondly, we concentrate our efforts on a four specific points in the phase diagram, with each point lying on a phase boundary. Lastly, we content ourselves with visual examination of crossing points instead of systematic fitting which would have required high statistics. The payoff for these choices is clear information about the evolution of the phase diagram at large system sizes.

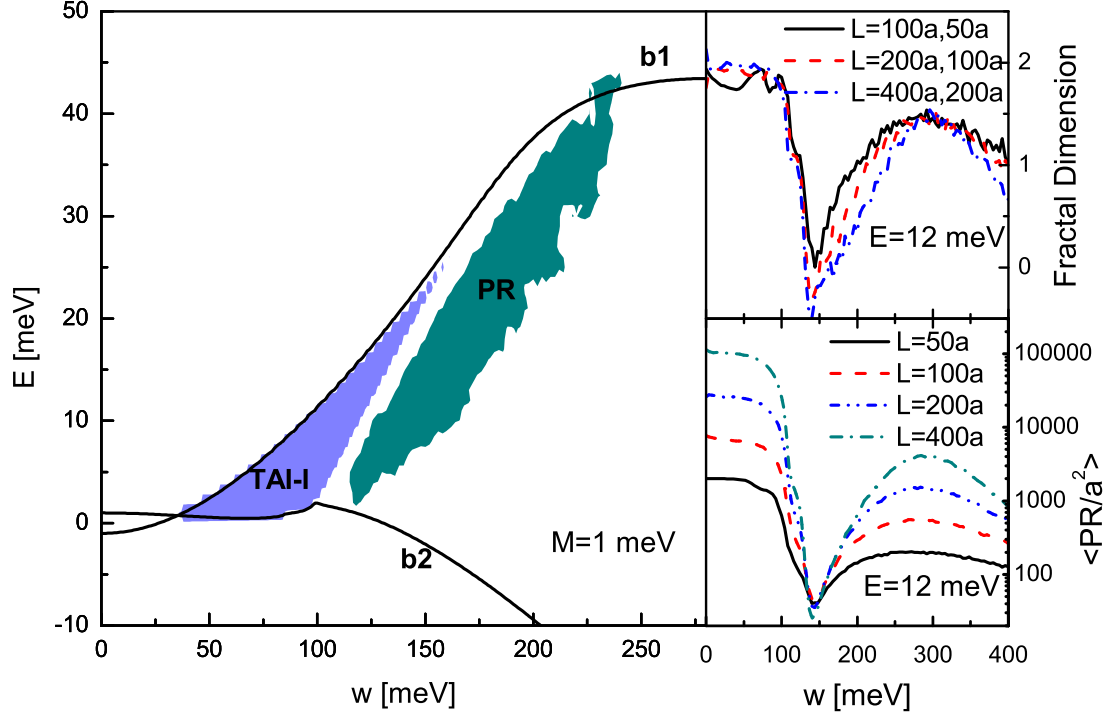


Figure 3.4: Eigenstate hyperlocalization near the mean-field band edge. Inside the colored ‘PR’ area the average PR is very small. (In this plot we show the region where $\langle PR \rangle \leq e^5 a^2 \approx 148 a^2$ at system size $L = 200a$.) If we omit surface states from the average, then we find that the bulk states are hyperlocalized in both the gapped TAI-I region and the PR region. Lines $b1$ and $b2$ show where the CPA-adjusted Fermi level crosses the CPA-adjusted band edges, and match well with the bulk hyperlocalized region. The lower right inset shows the average participation ratio at four system sizes, while the upper right inset shows the fractal dimension. The Fermi energy is fixed at $E_F = 12$ meV in both insets.

3.3.1 Transition from Bulk Conduction to the TAI Plateau

Figure 3.5 examines the boundary between the bulk conducting phase and the TAI conductance plateau, including both the gapped TAI-I scaling region and the ungapped TAI-II scaling region. Figure 3.5b shows the transition from bulk conduction to the ungapped TAI-II region. At this transition all of the bulk states become localized. There is a clear crossing point near $W \approx 200$ meV, indicating scale-invariant physics typical of disorder-induced phase transitions.

Unlike the TAI-II transition, the transition to the gapped TAI-I region (Figure 3.5a) is a meeting point. Moreover, our data at $L = 50, 100, 200, 400$, and $800a$ shows very clearly that the meeting point is converging to $W \approx 106$ meV. The conductance dip seen so clearly at $L = 50a$ shrinks and moves to the right; it is a finite size effect. The meeting point and its excellent convergence indicate that the gapped TAI-I physics has a finite length scale, and therefore point toward physics more complex than a simple bulk band edge. Bulk states inside a band gap have a decay length. This decay length is a function of the distance $E_F - E_{band}$ of the Fermi energy from the band edge, and diverges at the band edge where $E_F - E_{band} = 0$. Our data indicates that there is no such diverging length scale at the weak-disorder edge of the gapped TAI-I region.

Figures 3.5c and d show the second moment of the conductance at the transitions from bulk conductance to the TAI-I and TAI-II regions. In the bulk conducting phase the second moment is finite and increases with the system size. Both graphs show that $rms(G)$ converges to zero in the TAI conductance plateau. As the system size is increased the transition in $rms(G)$ sharpens and moves toward coinciding with the transition in $\langle G \rangle$. This corroborates our determination of the bulk-to-quantized phase transition, and also allows us to measure $\langle G \rangle$ precisely with small statistics.

Because our Hamiltonian is a member of the unitary symmetry class, we expect that the bulk Anderson transition - the extinction of bulk conduction - should move

toward zero disorder $W = 0$ as the system size is increased. Therefore we should see the conductance curves shift toward smaller disorder as the system size is increased. Moreover, in large enough systems the bulk Anderson transition should detach from the TAI conductance plateau, and one should see a ‘notch’ of zero conductance grow and separate the bulk conduction phase from the TAI conductance plateau. Figure 3.5a does not agree with these expectations - there is no evidence of any movement or notch at the edge of the gapped TAI-I region. The inset of Figure 3.5b indicates that the edge of the TAI-II region is moving, but the movement is quite small. There is no sign of a conductance notch anywhere, despite searches at system sizes as large as $L = 1120a$. We find no evidence that the weak-disorder boundary of the TAI conductance plateau can exist independently of a mobility edge. In summary, the transition from bulk conductance to the TAI conductance plateau is very stable under increases of the system size.

This stability is peculiar to the $2 - D$ square geometry which we study. With the exception of Ref. [67], all other studies of the TAI conductance have invariably calculated conduction along quasilinear strips which are much longer than their width. In this geometry bulk conduction is controlled by the ratio of the strip length to the localization length, while edge conduction is controlled by the ratio of the strip width to the localization length. As a result a $\langle G \rangle = 0$ conductance notch between the bulk and quantized phases is easy to reproduce. In a true $2 - D$ geometry the two ratios are identical, resulting in the notch-less physics which we observe.

3.3.2 Localization Transitions

Figure 3.6 shows the two localization transitions: the quantized-to-localized transition in panes a and c, and the bulk conducting-to-localized transition in panes b and d. The upper panes show closeups, while the insets show larger scales. The closeups show that the crossing points are ‘walking’ to weaker disorder because of finite size

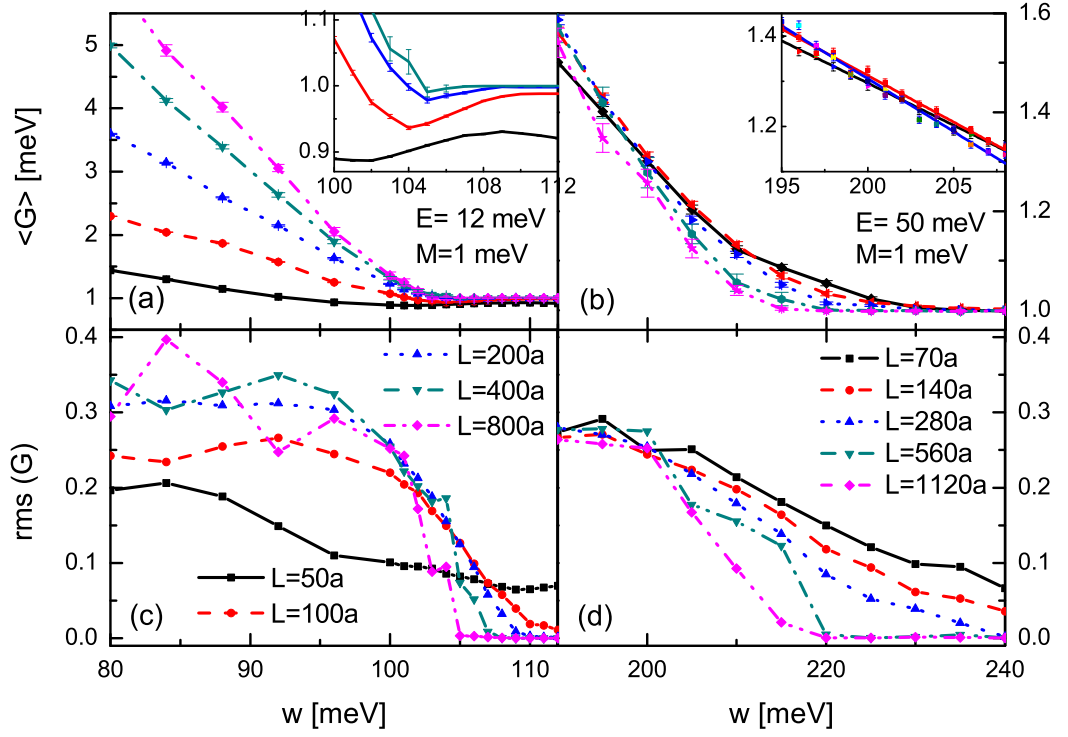


Figure 3.5: Phase transitions from the bulk conducting phase to the TAI-I and TAI-II scaling regions. Panes a and c show the transition to the gapped TAI-I scaling region, while panes b and d show the transition to the ungapped TAI-II scaling region. The insets show closeups of the conductance data. The straight lines in the upper right inset are least squares linear fits to the data.

effects. At the quantized-to-insulator transition the $L = 50, 100a$ crossing point is near $W \approx 380$ meV, the $L = 100, 200a$ crossing point is around $W \approx 343$ meV, and the $L = 200, 400a$ crossing point is at $W \approx 320$ meV. We can expect the true phase transition to be further to the left. In contrast, the bulk-to-insulator transition at $E = -15$ meV walks only ≈ 10 meV between the $L = 50, 100a$ and $L = 100, 200a$ crossing points. The improved stability at $E = -15$ meV may be caused by the larger density of states at that energy.

Figure 3.6c plots the second moment of the conductance, which forms a broad peak near the quantized-to-localized phase transition. The position of the peak seems to be less sensitive to finite size effects than the conductance crossing point. The peak grows more narrow as the system size is increased, suggesting that in the infinite volume limit the second moment is non-zero only at the phase transition. The peak is caused by bulk state delocalization, which allows the bulk states to connect and destroy the edge states.

Chen et al [115] calculated the logarithmic average of the bulk conductance at system sizes $70a \times 70a$, $100a \times 100a$, $130a \times 130a$. They used periodic boundary conditions and did not include the conductance of edge states. In the neighborhood of the quantized-insulator transition they found a finite ‘metallic’ region where $\langle \ln G \rangle$ increases, as is typical of a metal. They concluded that a metallic phase intervenes between the quantized phase and the insulating phase. In our judgement this conclusion is ill-founded. Our data near the quantized-insulator transition shows that the average conductance (including both bulk and edge states) is less than one at all $50 \leq L \leq 400a$ and converges to a step function. This implies that the bulk conductance is also less than one; the bulk does not become metallic. In fact Chen et al’s $\langle \ln G \rangle$ is always less than zero. Both their data and our data are consistent with the delocalization of a single bulk channel, which is necessary to destroy the edge states. It is likely that a careful calculation of the localization lengths associated

with several bulk channels would show that only one bulk channel delocalizes at the quantized-insulator phase transition.

The finite width of the region where the bulk channel is delocalized may be a finite-size effect, as is suggested by our data on the second moment $rms(G)$ and the fractal dimension d_2 . Both of these quantities have broad peaks near the phase transition, and the peaks become progressively more narrow as the system size is increased. If one calculated the width of the delocalized region at several system sizes, one should find that this region shrinks when the system size is increased. In an infinite system the delocalized region (and the peaks in $rms(G)$ and d_2) should have zero width and coincide with the quantized-insulator transition.

Lastly, Yamakage et al [69] studied systems of size $L = 16, 32, 64a$ and found a region between the quantized and insulating phases where the localization length increases with the system size, but only in a model where the s_z spin component is not conserved. The model which we are studying does conserve s_z , and Yamakage et al report that it exhibits no intermediate metallic phase.

3.3.3 Infinite Volume Limit of the Gapped TAI-I Scaling Region

Figure 3.7 shows the local density of states ρ at system sizes up to $L = 800a$. In much of the graph ρ is roughly constant as expected of bulk states; this is the ungapped TAI-II scaling region. In the interval $\approx 110 \text{ meV} \leq W \leq \approx 130 \text{ meV}$ ρ decreases as the system size increases from $L = 50a$ to $L = 100a$ to $L = 200a$. In most of this interval the $L = 50, 100, 200a$ curves are equally spaced because edge states obey $\rho \propto 1/L$. These signals allow us to distinguish the gapped TAI-I scaling region where there are many more edge states than bulk states.

As the system size increases, the region where ρ is changing shrinks, as does the region of $1/L$ edge scaling. We conclude that ρ converges to a small size-independent value indicating bulk states. This convergence is confirmed by the $L = 800a$ (PBC)

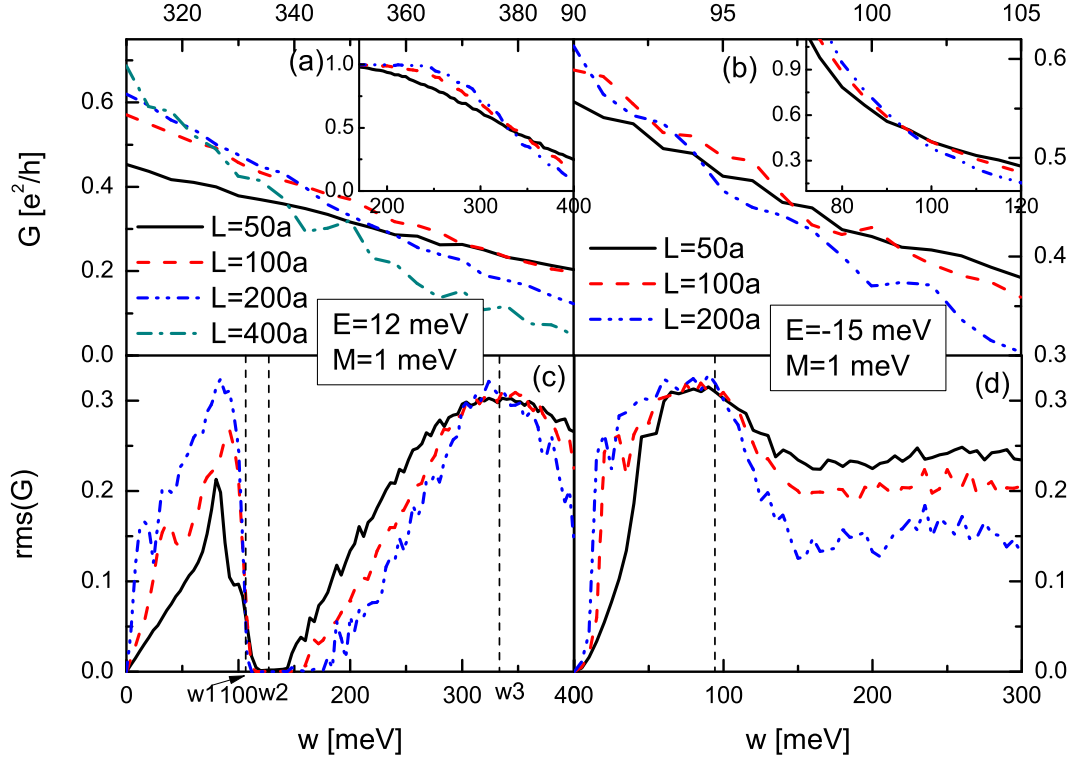


Figure 3.6: Anderson transitions to the localized phase. Panes a and c show the transition from the TAI conductance plateau to the insulating phase, while panes b and d show the transition from the bulk conducting phase to the insulating phase. The insets show the crossing points in a larger perspective. The vertical lines show the phase transition boundaries obtained using sizes $L = 50, 100, 200a$ (same as Figures 3.1 and 3.3).

curve obtained with periodic boundary conditions, which shows only the bulk DOS. (The minima of the PBC curves suffer from larger errors caused by the very small DOS.) The linear form of the bulk DOS on both sides of the TAI-I region indicates that the bulk DOS is exponentially small. In fact band gaps in disordered systems are always populated by localized intruder states from the bulk bands. This effect is called a Lifshitz tail, and is known to be exponentially small. In summary, the DOS is the sum of an edge $1/L$ contribution and an exponentially small bulk contribution from localized Lifshitz tail states.

Does any observable allow us to distinguish between the TAI-I and TAI-II scaling regions in infinite systems? Since the bulk Lifshitz tails overwhelm the edge states at large system sizes, a scaling analysis of ρ and $\langle d/L \rangle$ will show the gapped TAI-I region disappearing as the size is increased. However in infinite systems a hole in the bulk DOS will continue to mark the TAI-I region. The density of states in the TAI-I hole drops exponentially as one moves away from the band edges toward the center of the hole. Moreover we saw in Figure 3.5 that the TAI-I and TAI-II regions can be distinguished by their transition to the bulk conduction region: the TAI-II transition manifests scale invariance and a crossing point, while the TAI-I transition exhibits a meeting point and an absence of scale invariance. Lastly, our calculation of the $\langle PR \rangle$ with periodic boundary conditions (bulk states only) reveals that at the weak-disorder boundary the bulk states localize, and that inside the TAI-I region the PR descends to a plateau with a very small value $\langle PR \rangle \approx 10a^2$. The $\langle PR \rangle$ plateau extends over an interval of about ≈ 20 meV and includes the boundary between the TAI-I and TAI-II regions. This bulk localization is responsible for the TAI conductance plateau. Each of these observables - the hole in the DOS, the meeting point vs. crossing point, and the very small $\langle PR \rangle \approx 10a^2$ - distinguishes between the two TAI scaling regions.

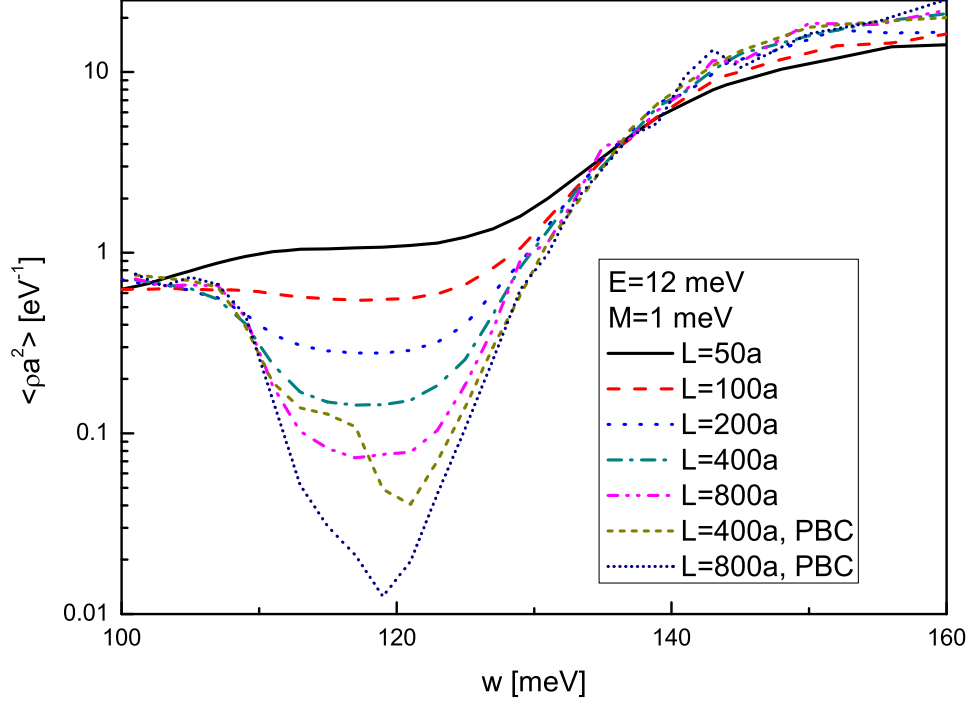


Figure 3.7: The TAI-I scaling region at large volumes. The density of states converges as the system size increases, starting at the edges of the TAI-I scaling region near $W \approx 110, 130$ meV and moving into the center of the scaling region. This convergence indicates that bulk states dominate the DOS in the infinite volume limit. The converged DOS agrees well with the ‘PBC’ lines, which were obtained with periodic boundary conditions and report the DOS of bulk states only. The converged value of the bulk DOS is roughly linear on both sides of the TAI-I scaling region, which indicates that the bulk DOS is exponentially small, as is typical of Lifshitz tails.

3.3.4 Conductance Distributions at the Phase Transitions

Figure 3.8 shows the conductance probability distribution at four points in the phase diagram. At disorder-induced phase transitions the conductance distribution is a critical quantity - it converges as the system size is increased, and is independent of microscopic details of models that belong to the same universality class. The critical conductance distribution has been determined precisely for both the integer quantum Hall system and for the quantum spin Hall (QSH) system. The dashed red lines in Figure 3.8 were already published in works by Kramer et al [128] and Kobayashi et al [129]. The authors systematically fitted their data to remove finite size effects, determined precisely the phase transition positions in the infinite-volume limit, and obtained data sets containing one million conductances. Here we compare those well known distributions with the TAI conductance distributions.

The solid black lines in Figure 3.8 display our data, which is noisy because our data sets contain only 20,000 conductances. This statistical error is dwarfed by our uncertainty about the true infinite-volume limit of the phase transitions. The conductance distribution can change very quickly as one moves through a phase transition. Unfortunately a precise determination of the phase transition would have required very thoughtful and systematic fitting of finite size effects, and very large data sets at many system sizes. Instead we did visual estimates of the crossing points using only a few system sizes. Therefore our data is valuable mainly for preliminary suggestions about which universality classes the TAI phase transitions may belong to.

We begin with the quantized-insulator transition, shown in Figure 3.8b. The essential physics here is that the edge states are destroyed while the bulk states are already localized. We compare our data to the integer quantum Hall transition because both models are unitary, and because Groth et al [67] suggested that both phase transitions lie in the same universality class. As we discussed in reference to Figure 3.6a, this transition has very large finite-size effects and the true transition

is likely to lie at a disorder strength smaller than ≈ 320 meV, which is the position of the $L = 200, 400a$ crossing point. We find that the $W = 308$ meV conductance distribution matches fairly well to the IQH distribution. It is possible that a precise determination of the phase transition would result in a perfect match to the IQH conductance distribution. As previously mentioned, we measure a fractal exponent $d_2 \approx 1.5$ on this phase boundary, which is consistent with the known IQH value.

Next we consider the transition from bulk conductance to the ungapped TAI-II scaling region, shown in Figure 3.8a. The essential physics here is that the bulk states localize while the edge states remain conducting. Unfortunately there is no metallic phase in the IQH system, so we compare the TAI distribution to the metal-quantized transition in the QSH system. Despite the fact that the QSH system belongs to the symplectic not unitary class, the two distributions have similar shapes, both at $W = 200$ meV (shown) and $W = 205$ meV (not shown).

Figures 3.8c,d show the Anderson transition from bulk conduction to the insulating phase at different values of the disorder $W = 90, 95$ meV. The essential physics here is that the bulk states localize and that there are no edge states. Our crossing point analysis (see Figure 3.6b) along the $E = -15$ meV line indicates that the infinite volume limit is at $W < \approx 94$ meV. Near here the conductance distribution changes very rapidly, perhaps because of the nearby tricritical point where the quantized region begins. At $W = 90$ meV the conductance distribution matches very well to the QSH metal-insulator transition, which is peculiar because the QSH system is symplectic while ours is unitary. At $W = 95$ meV it is similar to the IQH distribution when edge states have been removed by using periodic boundary conditions. The similarity is again perplexing, for the IQH transition is a point where the bulk states delocalize briefly, not where they move from extended to localized. A more precise determination of the Anderson transition is required to determine the true critical conductance distribution.

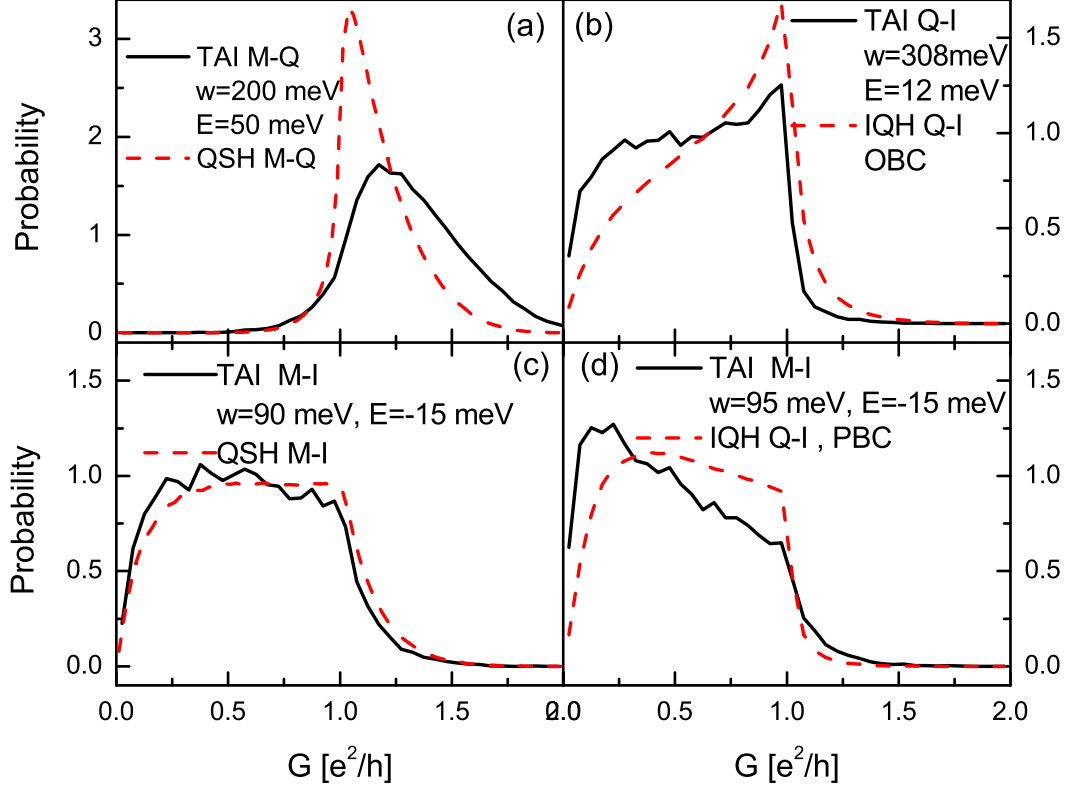


Figure 3.8: Conductance distributions at the TAI phase transitions. Pane a: the TAI bulk conduction-quantized transition, compared to the quantum spin Hall metal-quantized transition. Pane b: the TAI quantized-insulator transition, compared to the IQH with open boundary conditions. Pane c: the TAI bulk conduction-insulator transition at $W = 90$ meV, compared to the Quantum Spin Hall metal-insulator transition. Pane d: the TAI bulk conduction-insulator transition at $W = 95$ meV, compared to the IQH with periodic boundary conditions. We rescaled Kobayashi et al's QSH data by a factor of 2 ($P(G) \rightarrow 2P(G/2)$) because in our own calculations we report only $1/2$ of the total conductance of the 4×4 Hamiltonian - see the discussion in section 3.1.1. The system size is $L = 200a$ for all of our distributions.

3.4 Conclusion

In this paper we determined the TAI phase diagram at system sizes $L \leq 280a$ and studied its evolution in larger systems. While the TAI conductance plateau is caused by inversion of the bulk bands, it cannot be explained entirely by scattering (CPA) physics and a bulk band gap. A large portion of the conductance plateau lies in the ungapped TAI-II scaling region. When $L \leq 280a$ the gapped TAI-I scaling region is well described by the CPA, but in larger systems its density of states is dominated by Lifshitz tails of localized bulk states. We carefully studied the phase transitions in very large systems and excluded the possibility of extra metallic and insulating phases which had been reported in previous studies. We also reported broad peaks in the eigenstate size and fractal dimension that are centered near the quantized to insulating phase boundary and compared the TAI conductance distributions with known results for IQH and QSH systems.

APPENDIX: Numerical Errors in Determining the Phase Diagram

Our determination of the crossing points was based on visual comparison of observables at three system sizes, and included neither fitting the data to a finite size scaling function nor a precise mathematical estimate of errors. There are three error sources:

1. Finite-size effects. We used system sizes $L = 50, 100, 200a$ for determining all fixed- W crossing points (open boxes), and also for the $E = -15, 12, 35$ meV data points. At the remaining data points the sizes were $L = 70, 140$, and $280a$. Our phase diagram omits physics at scales greater than $L = 280a$, and includes finite size effects that are proportional to some small power of $1/L$. These effects cause the observed crossing point to be displaced from the position of the true phase transition; the observed crossing point ‘walks’ toward the correct value as the system size is increased. Figures 3.5 and 3.6 and the accompanying

discussion report our observations of this effect.

2. Statistical errors. Along the upper part of the quantized-insulator transition (filled boxes on line *eg2*) the finite size effects are so large that the statistical errors can be neglected. Along the lower part of this curve (open boxes on line *eg2*) the finite size effects are much smaller, of the same order as the statistical error. On the transition from bulk conductance to the ungapped TAI-II scaling region (line *eg1*) the finite size effects are so small that they are overwhelmed by the statistical errors. In the gapped TAI-I scaling region the fluctuations in G are essentially null, so on line *g1* the statistical error is negligible. Our estimation of the statistical errors is based on both calculation of the second moment of the observable and visual observation of fluctuations in our conductance curves. Our ensemble size depends on the system size. For all fixed- W crossing points and also the $E = -15, 12, 35$ meV data points, we used $N \geq 3000$ disorder realizations at $L = 50a$ and $N \geq 1000, 500$ realizations at $L = 100, 200a$. At the other fixed- E data points we used $N = 800, 800, 100$ realizations at sizes $L = 70, 140$, and $280a$.
3. Errors from doping the leads. As we mentioned in section 3.1.1, if we leave the leads undoped then they force the conductance to zero at $|E| \leq M = 1$ meV. At energies neighboring $|E| \leq M = 1$ meV there is a finite size effect: at small system sizes the conductance hole is widened. Therefore we have doped the leads to $E = 25$ meV at all fixed- W data points (the open boxes), and also in Figure 3.1. We examined the doping-induced error by calculating crossing points at $W = 200$ meV and $E = 10, 12$ meV both with doped and undoped leads. Our results indicate that the effect of doping is minimal on line *g1*, on the fixed- W data points (open boxes), and on Figure 3.1. The doped fixed- W data also satisfies an important consistency check: it reproduces correctly data

points along the lower edge $g2$ of the gapped TAI-I scaling region. Doping has a much more pronounced effect on line $eg1$, where it shifts the $W = 200$ meV data point from $E = 50$ meV to $E = 42$ meV, but happily all of our data points on $eg1$ were obtained from undoped data.

The content of this chapter has been accepted to publish in Phys. Rev. B. 85, 195140 (2012).

CHAPTER 4

CONCLUSIONS

In this dissertation, two kinds of systems containing disorder are studied. Firstly, we studied bilayer and trilayer graphene nanoribbons where the disorder was distributed in the bottom layer only. The longitudinal conductance was calculated using tight-binding Green's function when perpendicular bias voltage was applied. The conductance shows disorder and voltage dependence. We then calculated the ratio of conductances from opposite bias voltages at different disorder strength for both zigzag and armchair edged bilayer graphene nanoribbons. It is shown that the stronger disorder strength and larger bias voltage are preferred. No big difference were observed between the edge types. The behaviors of the conductance ratio in bilayer graphene are well explained by the low energy four band model and the properties of the conductance ratio in trilayer graphene are predicted. The study on trilayer graphene showed that the conductance ratios of ABA stacking are comparable with that of ABC stacking. This indicates that energy gap is not necessary to get a high conductance ratio. High conductance ratio means good field effect transistor. From our study, we believe that new kind of field effect transistor based on the disordered multilayer graphene is promising. Secondly, we studied the disordered topological Anderson insulator (TAI) of 2D $HgTe$ system theoretically. The TAI phase diagram at system sizes $L \leq 280a$ was obtained by finite size scaling. In studying of the TAI phase structure, we found that normalized band gap is not essential to get the TAI phase. There are two regions called TAI phase: TAI-I related to the band gap and TAI-II without band gap. The Born Approximation can not entirely explain the

physics of TAI. The evolution in larger systems was then studied. Its density of states is dominated by Lifshitz tails of localized bulk states. We carefully studied the phase transitions in very large systems and excluded the possibility of extra metallic and insulating phases. We reported broad peaks in the eigenstate size and fractal dimension that are centered near the quantized to insulating phase boundary. Four kinds of phase transitions were focused on: (1) from bulk conductor to quantized topological insulator without a band gap, (2) from bulk conductor to quantized topological insulator with a band gap, (3) from quantized topological insulator to normal insulator, and (4) from bulk conductor to bulk insulator. We compared the TAI conductance probability distributions with known results for IQH and QSH systems and found they fairly coincide with each other.

BIBLIOGRAPHY

- [1] B. Kramer and A. MacKinnon, “Localization: theory and experiment,” *Reports on Progress in Physics*, vol. 56, no. 12, p. 1469, 1993.
- [2] E. Abrahams, P. W. Anderson, D. C. Licciardello, and T. V. Ramakrishnan, “Scaling theory of localization: Absence of quantum diffusion in two dimensions,” *Phys. Rev. Lett.*, vol. 42, pp. 673–676, Mar 1979.
- [3] M. Wilson, “Electrons in atomically thin carbon sheets behave like massless particles,” *Physics Today*, vol. 59, no. 1, pp. 21–23, 2006.
- [4] P. W. Anderson, “Absence of diffusion in certain random lattices,” *Phys. Rev.*, vol. 109, pp. 1492–1505, Mar 1958.
- [5] N. Mott, “Conduction in glasses containing transition metal ions,” *Journal of Non-Crystalline Solids*, vol. 1, no. 1, pp. 1 – 17, 1968.
- [6] F. Evers and A. Mirlin, “Anderson transitions,” *Reviews of Modern Physics*, vol. 80, no. 4, p. 1355, 2008.
- [7] D. Thouless, “Electrons in disordered systems and the theory of localization,” *Physics Reports*, vol. 13, no. 3, pp. 93 – 142, 1974.
- [8] E. Abrahams, S. V. Kravchenko, and M. P. Sarachik, “Metallic behavior and related phenomena in two dimensions,” *Rev. Mod. Phys.*, vol. 73, pp. 251–266, Mar 2001.
- [9] L. A. Tracy, E. H. Hwang, K. Eng, G. A. Ten Eyck, E. P. Nordberg, K. Childs, M. S. Carroll, M. P. Lilly, and S. Das Sarma, “Observation of percolation-

- induced two-dimensional metal-insulator transition in a si mosfet,” *Phys. Rev. B*, vol. 79, p. 235307, Jun 2009.
- [10] E. Miranda, V. Dobrosavljević, and G. Kotliar, “Disorder-driven non-fermi-liquid behavior in kondo alloys,” *Phys. Rev. Lett.*, vol. 78, pp. 290–293, Jan 1997.
 - [11] A. Punnoose and A. M. Finkel’stein, “Metal-insulator transition in disordered two-dimensional electron systems,” *Science*, vol. 310, no. 5746, pp. 289–291, 2005.
 - [12] P. B. Chakraborty, K. Byczuk, and D. Vollhardt, “Interacting lattice electrons with disorder in two dimensions: Numerical evidence for a metal-insulator transition with a universal critical conductivity,” *Phys. Rev. B*, vol. 84, p. 035121, Jul 2011.
 - [13] A. Geim and K. Novoselov, “The rise of graphene,” *Nature materials*, vol. 6, no. 3, pp. 183–191, 2007.
 - [14] R. Peierls, “Quelques propriétés typiques des corps solides,” *Ann. Inst. Henri Poincaré*, vol. 5, no. 3, pp. 177–222, 1935.
 - [15] J. Venables, G. Spiller, and M. Hanbucken, “Nucleation and growth of thin films,” *Reports on Progress in Physics*, vol. 47, p. 399, 1984.
 - [16] R. Mas-Ballesté, C. Gómez-Navarro, J. Gómez-Herrero, and F. Zamora, “2D materials: to graphene and beyond,” *Nanoscale*, vol. 3, no. 1, pp. 20–30, 2011.
 - [17] C. Lee, X. Wei, J. Kysar, and J. Hone, “Measurement of the elastic properties and intrinsic strength of monolayer graphene,” *Science*, vol. 321, no. 5887, pp. 385–388, 2008.

- [18] D. Abergel, V. Apalkov, J. Berashevich, K. Ziegler, and T. Chakraborty, “Properties of graphene: a theoretical perspective,” *Advances in Physics*, vol. 59, no. 4, pp. 261–482, 2010.
- [19] K. Bourzac, “Electronics: Back to analogue,” *Nature*, vol. 483, no. 7389, pp. S34–S36, 2012.
- [20] A. Balandin, S. Ghosh, W. Bao, I. Calizo, D. Teweldebrhan, F. Miao, and C. Lau, “Superior thermal conductivity of single-layer graphene,” *Nano Letters*, vol. 8, no. 3, pp. 902–907, 2008.
- [21] F. Varchon, R. Feng, J. Hass, X. Li, B. N. Nguyen, C. Naud, P. Mallet, J.-Y. Veuillen, C. Berger, E. H. Conrad, and L. Magaud, “Electronic structure of epitaxial graphene layers on sic: Effect of the substrate,” *Phys. Rev. Lett.*, vol. 99, p. 126805, Sep 2007.
- [22] M. Ishigami, J. H. Chen, W. G. Cullen, M. S. Fuhrer, and E. D. Williams, “Atomic structure of graphene on SiO₂,” *Nano Letters*, vol. 7, no. 6, pp. 1643–1648, 2007.
- [23] C. Dean, A. Young, I. Meric, C. Lee, L. Wang, S. Sorgenfrei, K. Watanabe, T. Taniguchi, P. Kim, K. Shepard, *et al.*, “Boron nitride substrates for high-quality graphene electronics,” *Nature nanotechnology*, vol. 5, no. 10, pp. 722–726, 2010.
- [24] G. Eda, H. Emrah Unalan, N. Rupesinghe, G. Amaratunga, and M. Chhowalla, “Field emission from graphene based composite thin films,” *Applied Physics Letters*, vol. 93, no. 23, pp. 233502–233502, 2008.
- [25] F. Schedin, A. Geim, S. Morozov, E. Hill, P. Blake, M. Katsnelson, and K. Novoselov, “Detection of individual gas molecules adsorbed on graphene,” *Nature materials*, vol. 6, no. 9, pp. 652–655, 2007.

- [26] S. Gowtham, R. Scheicher, R. Ahuja, R. Pandey, and S. Karna, “Physisorption of nucleobases on graphene: density-functional calculations,” *Physical Review B*, vol. 76, no. 3, p. 033401, 2007.
- [27] N. Savage, “Come into the light,” *Nature*, vol. 483, no. 7389, pp. S38–S39, 2012.
- [28] C. Schmidt, “Bioelectronics: The bionic material,” *Nature*, vol. 483, no. 7389, pp. S37–S37, 2012.
- [29] J. Lee, S. Lee, J. Ahn, S. Kim, J. Wilson, P. John, *et al.*, “The growth of aa graphite on (111) diamond,” *Journal of Chemical Physics*, vol. 129, no. 23, p. 234709, 2008.
- [30] X. Chang, Y. Ge, and J. Dong, “Ripples of AA and AB stacking bilayer graphenes,” *The European Physical Journal B-Condensed Matter and Complex Systems*, vol. 78, no. 1, pp. 103–109, 2010.
- [31] T. Ohta, A. Bostwick, T. Seyller, K. Horn, and E. Rotenberg, “Controlling the electronic structure of bilayer graphene,” *Science*, vol. 313, no. 5789, pp. 951–954, 2006.
- [32] Y. Zhang, T. Tang, C. Girit, Z. Hao, M. Martin, A. Zettl, M. Crommie, Y. Shen, and F. Wang, “Direct observation of a widely tunable bandgap in bilayer graphene,” *Nature*, vol. 459, no. 7248, pp. 820–823, 2009.
- [33] W. Bao, L. Jing, J. Velasco Jr, Y. Lee, G. Liu, D. Tran, B. Standley, M. Aykol, S. Cronin, D. Smirnov, *et al.*, “Stacking-dependent band gap and quantum transport in trilayer graphene,” *Nature Physics*, vol. 7, no. 12, pp. 948–952, 2011.

- [34] K. Novoselov, A. Geim, S. Morozov, D. Jiang, Y. Zhang, S. Dubonos, I. Grigorieva, and A. Firsov, “Electric field effect in atomically thin carbon films,” *Science*, vol. 306, no. 5696, pp. 666–669, 2004.
- [35] A. Ferrari, J. Meyer, V. Scardaci, C. Casiraghi, M. Lazzeri, F. Mauri, S. Piscanec, D. Jiang, K. Novoselov, S. Roth, *et al.*, “Raman spectrum of graphene and graphene layers,” *Physical Review Letters*, vol. 97, no. 18, p. 187401, 2006.
- [36] M. Dresselhaus and G. Dresselhaus, “Intercalation compounds of graphite,” *Advances in Physics*, vol. 30, no. 2, pp. 139–326, 1981.
- [37] S. Park and R. Ruoff, “Chemical methods for the production of graphenes,” *Nature nanotechnology*, vol. 4, no. 4, pp. 217–224, 2009.
- [38] D. Dikin, S. Stankovich, E. Zimney, R. Piner, G. Dommett, G. Evmenenko, S. Nguyen, and R. Ruoff, “Preparation and characterization of graphene oxide paper,” *Nature*, vol. 448, no. 7152, pp. 457–460, 2007.
- [39] G. Che, B. Lakshmi, C. Martin, E. Fisher, and R. Ruoff, “Chemical vapor deposition based synthesis of carbon nanotubes and nanofibers using a template method,” *Chemistry of Materials*, vol. 10, no. 1, pp. 260–267, 1998.
- [40] K. Kim, Y. Zhao, H. Jang, S. Lee, J. Kim, K. Kim, J. Ahn, P. Kim, J. Choi, and B. Hong, “Large-scale pattern growth of graphene films for stretchable transparent electrodes,” *Nature*, vol. 457, no. 7230, pp. 706–710, 2009.
- [41] P. Sutter, J. Flege, and E. Sutter, “Epitaxial graphene on ruthenium,” *Nature materials*, vol. 7, no. 5, pp. 406–411, 2008.
- [42] D. Stradi, S. Barja, C. Díaz, M. Garnica, B. Borca, J. Hinarejos, D. Sánchez-Portal, M. Alcamí, A. Arnau, A. Vázquez de Parga, *et al.*, “Role of dispersion

- forces in the structure of graphene monolayers on ru surfaces,” *Physical review letters*, vol. 106, no. 18, p. 186102, 2011.
- [43] J. Moore, “The birth of topological insulators,” *Nature*, vol. 464, no. 7286, pp. 194–198, 2010.
 - [44] D. J. Thouless, M. Kohmoto, M. P. Nightingale, and M. den Nijs, “Quantized hall conductance in a two-dimensional periodic potential,” *Phys. Rev. Lett.*, vol. 49, pp. 405–408, Aug 1982.
 - [45] C. L. Kane and E. J. Mele, “ Z_2 topological order and the quantum spin hall effect,” *Phys. Rev. Lett.*, vol. 95, p. 146802, Sep 2005.
 - [46] J. E. Moore and L. Balents, “Topological invariants of time-reversal-invariant band structures,” *Phys. Rev. B*, vol. 75, p. 121306, Mar 2007.
 - [47] R. Roy, “ Z_2 classification of quantum spin hall systems: An approach using time-reversal invariance,” *Phys. Rev. B*, vol. 79, p. 195321, May 2009.
 - [48] X.-L. Qi, T. L. Hughes, and S.-C. Zhang, “Topological field theory of time-reversal invariant insulators,” *Phys. Rev. B*, vol. 78, p. 195424, Nov 2008.
 - [49] K. v. Klitzing, G. Dorda, and M. Pepper, “New method for high-accuracy determination of the fine-structure constant based on quantized hall resistance,” *Phys. Rev. Lett.*, vol. 45, pp. 494–497, Aug 1980.
 - [50] C. L. Kane and E. J. Mele, “Quantum spin hall effect in graphene,” *Phys. Rev. Lett.*, vol. 95, p. 226801, Nov 2005.
 - [51] B. A. Bernevig and S.-C. Zhang, “Quantum spin hall effect,” *Phys. Rev. Lett.*, vol. 96, p. 106802, Mar 2006.
 - [52] S. Murakami, N. Nagaosa, and S.-C. Zhang, “Dissipationless quantum spin current at room temperature,” *Science*, vol. 301, no. 5638, pp. 1348–1351, 2003.

- [53] X.-L. Qi, Y.-S. Wu, and S.-C. Zhang, “Topological quantization of the spin hall effect in two-dimensional paramagnetic semiconductors,” *Phys. Rev. B*, vol. 74, p. 085308, Aug 2006.
- [54] R. Roy, “Topological phases and the quantum spin hall effect in three dimensions,” *Phys. Rev. B*, vol. 79, p. 195322, May 2009.
- [55] D. Hsieh, D. Qian, L. Wray, Y. Xia, Y. Hor, R. Cava, and M. Hasan, “A topological dirac insulator in a quantum spin hall phase,” *Nature*, vol. 452, no. 7190, pp. 970–974, 2008.
- [56] L. Fu, C. L. Kane, and E. J. Mele, “Topological insulators in three dimensions,” *Phys. Rev. Lett.*, vol. 98, p. 106803, Mar 2007.
- [57] Y.-q. Li, K.-h. Wu, J.-r. Shi, and X.-c. Xie, “Electron transport properties of three-dimensional topological insulators,” *Frontiers of Physics*, vol. 7, pp. 165–174, 2012.
- [58] B. A. Bernevig, T. L. Hughes, and S.-C. Zhang, “Quantum spin hall effect and topological phase transition in hgte quantum wells,” *Science*, vol. 314, no. 5806, pp. 1757–1761, 2006.
- [59] M. Knig, S. Wiedmann, C. Brne, A. Roth, H. Buhmann, L. W. Molenkamp, X.-L. Qi, and S.-C. Zhang, “Quantum spin hall insulator state in hgte quantum wells,” *Science*, vol. 318, no. 5851, pp. 766–770, 2007.
- [60] L. Fu and C. L. Kane, “Topological insulators with inversion symmetry,” *Phys. Rev. B*, vol. 76, p. 045302, Jul 2007.
- [61] H. Zhang, C. Liu, X. Qi, X. Dai, Z. Fang, and S. Zhang, “Topological insulators in Bi_2Se_3 , Bi_2Te_3 and Sb_2Te_3 with a single dirac cone on the surface,” *Nature Physics*, vol. 5, no. 6, pp. 438–442, 2009.

- [62] Y. Xia, D. Qian, D. Hsieh, L. Wray, A. Pal, H. Lin, A. Bansil, D. Grauer, Y. Hor, R. Cava, *et al.*, “Observation of a large-gap topological-insulator class with a single dirac cone on the surface,” *Nature Physics*, vol. 5, no. 6, pp. 398–402, 2009.
- [63] Y. L. Chen, J. G. Analytis, J.-H. Chu, Z. K. Liu, S.-K. Mo, X. L. Qi, H. J. Zhang, D. H. Lu, X. Dai, Z. Fang, S. C. Zhang, I. R. Fisher, Z. Hussain, and Z.-X. Shen, “Experimental realization of a three-dimensional topological insulator, Bi_2Te_3 ,” *Science*, vol. 325, no. 5937, pp. 178–181, 2009.
- [64] S. Raghu, X.-L. Qi, C. Honerkamp, and S.-C. Zhang, “Topological mott insulators,” *Phys. Rev. Lett.*, vol. 100, p. 156401, Apr 2008.
- [65] Z. Wang, X.-L. Qi, and S.-C. Zhang, “Topological order parameters for interacting topological insulators,” *Phys. Rev. Lett.*, vol. 105, p. 256803, Dec 2010.
- [66] J. Li, R. Chu, J. Jain, and S. Shen, “Topological anderson insulator,” *Physical review letters*, vol. 102, no. 13, p. 136806, 2009.
- [67] C. Groth, M. Wimmer, A. Akhmerov, J. Tworzydło, and C. Beenakker, “Theory of the topological anderson insulator,” *Physical review letters*, vol. 103, no. 19, p. 196805, 2009.
- [68] E. Prodan, “Three-dimensional phase diagram of disordered HgTe/CdTe quantum spin-hall wells,” *Physical Review B*, vol. 83, no. 19, p. 195119, 2011.
- [69] A. Yamakage, K. Nomura, K. Imura, and Y. Kuramoto, “Disorder-induced multiple transition involving Z_2 topological insulator,” *Journal of the Physical Society of Japan*, vol. 80, no. 5, 2011.

- [70] Y. Zhang, R. Chu, F. Zhang, and S. Shen, “Localization and mobility gap in the topological anderson insulator,” *Physical Review B*, vol. 85, no. 3, p. 035107, 2012.
- [71] X.-L. Qi and S.-C. Zhang, “Topological insulators and superconductors,” *Rev. Mod. Phys.*, vol. 83, pp. 1057–1110, Oct 2011.
- [72] L. Fu and C. L. Kane, “Time reversal polarization and a Z_2 adiabatic spin pump,” *Phys. Rev. B*, vol. 74, p. 195312, Nov 2006.
- [73] T. Taychatanapat and P. Jarillo-Herrero, “Electronic transport in dual-gated bilayer graphene at large displacement fields,” *Phys. Rev. Lett.*, vol. 105, p. 166601, Oct 2010.
- [74] E. V. Castro, K. S. Novoselov, S. V. Morozov, N. M. R. Peres, J. M. B. L. dos Santos, J. Nilsson, F. Guinea, A. K. Geim, and A. H. C. Neto, “Biased bilayer graphene: Semiconductor with a gap tunable by the electric field effect,” *Phys. Rev. Lett.*, vol. 99, p. 216802, Nov 2007.
- [75] J. Oostinga, H. Heersche, X. Liu, A. Morpurgo, and L. Vandersypen, “Gate-induced insulating state in bilayer graphene devices,” *Nature materials*, vol. 7, no. 2, pp. 151–157, 2008.
- [76] E. McCann, “Asymmetry gap in the electronic band structure of bilayer graphene,” *Phys. Rev. B*, vol. 74, no. 16, p. 161403, 2006.
- [77] H. Min, B. Sahu, S. K. Banerjee, and A. H. MacDonald, “*Ab initio* theory of gate induced gaps in graphene bilayers,” *Phys. Rev. B*, vol. 75, p. 155115, Apr 2007.

- [78] E. K. Yu, D. A. Stewart, and S. Tiwari, “*Ab initio* study of polarizability and induced charge densities in multilayer graphene films,” *Phys. Rev. B*, vol. 77, p. 195406, May 2008.
- [79] F. Xia, D. Farmer, Y. Lin, and P. Avouris, “Graphene field-effect transistors with high on/off current ratio and large transport band gap at room temperature,” *Nano letters*, vol. 10, no. 2, pp. 715–718, 2010.
- [80] G. Fiori and G. Iannaccone, “On the possibility of tunable-gap bilayer graphene fet,” *Electron Device Letters, IEEE*, vol. 30, no. 3, pp. 261–264, 2009.
- [81] S. Kumar and J. Guo, “Multilayer graphene under vertical electric field,” *Appl. Phys. Lett*, vol. 98, p. 222101, 2011.
- [82] C. Lui, Z. Li, K. Mak, E. Cappelluti, and T. Heinz, “Observation of an electrically tunable band gap in trilayer graphene,” *Nature Physics*, vol. 7, no. 12, pp. 944–947, 2011.
- [83] A. Yacoby, “Graphene: Tri and tri again,” *Nature Physics*, vol. 7, no. 12, pp. 925–926, 2011.
- [84] M. Koshino and E. McCann, “Gate-induced interlayer asymmetry in ab-stacked trilayer graphene,” *Phys. Rev. B*, vol. 79, no. 12, p. 125443, 2009.
- [85] E. A. Henriksen, D. Nandi, and J. P. Eisenstein, “Quantum hall effect and semimetallic behavior of dual-gated ab-stacked trilayer graphene,” *Phys. Rev. X*, vol. 2, p. 011004, Jan 2012.
- [86] H. Min and A. H. MacDonald, “Electronic structure of multilayer graphene,” *Progr. Theoret. Phys. Suppl.*, vol. 176, p. 227, 2008.
- [87] F. Guinea, A. H. Castro Neto, and N. M. R. Peres, “Electronic states and landau levels in graphene stacks,” *Phys. Rev. B*, vol. 73, p. 245426, Jun 2006.

- [88] F. Zhang, B. Sahu, H. Min, and A. H. MacDonald, “Band structure of *abc*-stacked graphene trilayers,” *Phys. Rev. B*, vol. 82, p. 035409, Jul 2010.
- [89] A. A. Avetisyan, B. Partoens, and F. M. Peeters, “Electric-field control of the band gap and fermi energy in graphene multilayers by top and back gates,” *Phys. Rev. B*, vol. 80, p. 195401, Nov 2009.
- [90] S. Jhang, M. Craciun, S. Schmidmeier, S. Tokumitsu, S. Russo, M. Yamamoto, Y. Skourski, J. Wosnitza, S. Tarucha, J. Eroms, and C. Strunk, “Stacking-order dependent transport properties of trilayer graphene,” *Phys. Rev. B*, vol. 84, no. 16, p. 161408, 2011.
- [91] M. Craciun, S. Russo, M. Yamamoto, J. Oostinga, A. Morpurgo, and S. Tarucha, “Trilayer graphene is a semimetal with a gate-tunable band overlap,” *Nature nanotechnology*, vol. 4, no. 6, pp. 383–388, 2009.
- [92] Y. Shi, X. Dong, P. Chen, J. Wang, and L.-J. Li, “Effective doping of single-layer graphene from underlying SiO₂ substrates,” *Phys. Rev. B*, vol. 79, p. 115402, Mar 2009.
- [93] J.-N. Fuchs and P. Lederer, “Spontaneous parity breaking of graphene in the quantum hall regime,” *Phys. Rev. Lett.*, vol. 98, p. 016803, Jan 2007.
- [94] Y.-J. Kang, J. Kang, and K. J. Chang, “Electronic structure of graphene and doping effect on SiO₂,” *Phys. Rev. B*, vol. 78, p. 115404, Sep 2008.
- [95] S. Zhou, G. Gweon, A. Fedorov, P. First, W. De Heer, D. Lee, F. Guinea, A. Neto, and A. Lanzara, “Substrate-induced bandgap opening in epitaxial graphene,” *Nature Materials*, vol. 6, no. 10, pp. 770–775, 2007.

- [96] G. Giovannetti, P. A. Khomyakov, G. Brocks, P. J. Kelly, and J. van den Brink, “Substrate-induced band gap in graphene on hexagonal boron nitride: *Ab initio* density functional calculations,” *Phys. Rev. B*, vol. 76, p. 073103, Aug 2007.
- [97] G. Giovannetti, P. A. Khomyakov, G. Brocks, V. M. Karpan, J. van den Brink, and P. J. Kelly, “Doping graphene with metal contacts,” *Phys. Rev. Lett.*, vol. 101, p. 026803, Jul 2008.
- [98] J. Meyer, A. Geim, M. Katsnelson, K. Novoselov, T. Booth, and S. Roth, “The structure of suspended graphene sheets,” *Nature*, vol. 446, no. 7131, pp. 60–63, 2007.
- [99] R. Weitz, M. Allen, B. Feldman, J. Martin, and A. Yacoby, “Broken-symmetry states in doubly gated suspended bilayer graphene,” *Science*, vol. 330, no. 6005, pp. 812–816, 2010.
- [100] J. Velasco Jr, L. Jing, W. Bao, Y. Lee, P. Kratz, V. Aji, M. Bockrath, C. Lau, C. Varma, R. Stillwell, D. Smirnov, F. Zhang, J. Jung, and M. A. H., “Transport spectroscopy of symmetry-broken insulating states in bilayer graphene,” *Nature Nanotechnology*, vol. 7, no. 3, pp. 156–160, 2012.
- [101] T. Khodkov, F. Withers, D. Christopher Hudson, M. Felicia Craciun, and S. Russo, “Electrical transport in suspended and double gated trilayer graphene,” *Appl. Phys. Lett.*, vol. 100, no. 1, pp. 013114–013114, 2012.
- [102] G. Engdahl, *Handbook of giant magnetostrictive materials*. Academic Pr, 2000.
- [103] J. Nilsson, A. H. Castro Neto, F. Guinea, and N. M. R. Peres, “Electronic properties of bilayer and multilayer graphene,” *Phys. Rev. B*, vol. 78, p. 045405, Jul 2008.

- [104] Z. Qiao, W.-K. Tse, H. Jiang, Y. Yao, and Q. Niu, “Two-dimensional topological insulator state and topological phase transition in bilayer graphene,” *Phys. Rev. Lett.*, vol. 107, p. 256801, Dec 2011.
- [105] A. H. Castro Neto, F. Guinea, N. M. R. Peres, K. S. Novoselov, and A. K. Geim, “The electronic properties of graphene,” *Rev. Mod. Phys.*, vol. 81, pp. 109–162, Jan 2009.
- [106] W. Long, Q.-f. Sun, and J. Wang, “Disorder-induced enhancement of transport through graphene p-n junctions,” *Phys. Rev. Lett.*, vol. 101, p. 166806, Oct 2008.
- [107] S. Datta, *Electronic transport in mesoscopic systems*. Cambridge Univ Pr, 1995.
- [108] H. Jiang, S. Cheng, Q.-f. Sun, and X. C. Xie, “Topological insulator: A new quantized spin hall resistance robust to dephasing,” *Phys. Rev. Lett.*, vol. 103, p. 036803, Jul 2009.
- [109] M. Z. Hasan and C. L. Kane, “Colloquium: Topological insulators,” *Rev. Mod. Phys.*, vol. 82, pp. 3045–3067, Nov 2010.
- [110] X. Qi and S. Zhang, “The quantum spin hall effect and topological insulators,” *Physics Today*, vol. 63, no. 1, pp. 33–38, 2010.
- [111] C. Liu, X. Qi, H. Zhang, X. Dai, Z. Fang, and S. Zhang, “Model hamiltonian for topological insulators,” *Physical Review B*, vol. 82, no. 4, p. 045122, 2010.
- [112] H. Jiang, L. Wang, Q.-f. Sun, and X. C. Xie, “Numerical study of the topological anderson insulator in HgTe/CdTe quantum wells,” *Phys. Rev. B*, vol. 80, p. 165316, Oct 2009.
- [113] P. Soven, “Coherent-potential model of substitutional disordered alloys,” *Physical Review*, vol. 156, no. 3, p. 809, 1967.

- [114] D. W. Taylor, “Vibrational properties of imperfect crystals with large defect concentrations,” *Phys. Rev.*, vol. 156, pp. 1017–1029, Apr 1967.
- [115] L. Chen, Q. Liu, X. Lin, X. Zhang, and X. Jiang, “Evolutions of helical edge states in disordered HgTe/CdTe quantum wells,” *Arxiv preprint arXiv:1106.4103*, 2011.
- [116] H. Guo, G. Rosenberg, G. Refael, and M. Franz, “Topological anderson insulator in three dimensions,” *Physical review letters*, vol. 105, no. 21, p. 216601, 2010.
- [117] B. Bernevig, T. Hughes, and S. Zhang, “Quantum spin hall effect and topological phase transition in hgte quantum wells,” *Science*, vol. 314, no. 5806, pp. 1757–1761, 2006.
- [118] M. Onoda, Y. Avishai, and N. Nagaosa, “Localization in a quantum spin hall system,” *Physics Review Letters*, vol. 98, p. 076802, 2007.
- [119] H. Obuse, A. Furusaki, S. Ryu, and C. Mudry, “Two-dimensional spin-filtered chiral network model for the Z_2 quantum spin-hall effect,” *Physics Review B*, vol. 76, p. 075301, 2007.
- [120] C. Caroli, R. Combescot, P. Nozieres, and D. Saint-James, “Direct calculation of the tunneling current,” *Journal of Physics C: Solid State Physics*, vol. 4, p. 916, 1971.
- [121] Y. Meir and N. Wingreen, “Landauer formula for the current through an interacting electron region,” *Physical review letters*, vol. 68, no. 16, pp. 2512–2515, 1992.

- [122] M. P. L. Sancho, J. M. L. Sancho, J. M. L. Sancho, and J. Rubio, “Highly convergent schemes for the calculation of bulk and surface green functions,” *Journal of Physics F: Metal Physics*, vol. 15, no. 4, p. 851, 1985.
- [123] K. Slevin and T. Ohtsuki, “Critical exponent for the quantum hall transition,” *Phys. Rev. B*, vol. 80, p. 041304, Jul 2009.
- [124] B. Huckestein and L. Schweitzer, “Relation between the correlation dimensions of multifractal wave functions and spectral measures in integer quantum hall systems,” *Physical review letters*, vol. 72, no. 5, pp. 713–716, 1994.
- [125] T. Terao, T. Nakayama, and H. Aoki, “Multifractality of the quantum hall wave functions in higher landau levels,” *Phys. Rev. B*, vol. 54, pp. 10350–10353, Oct 1996.
- [126] R. Klesse and M. Metzler, “Spectral compressibility at the metal-insulator transition of the quantum hall effect,” *Phys. Rev. Lett.*, vol. 79, pp. 721–724, Jul 1997.
- [127] B. Huckestein and R. Klesse, “Wave-packet dynamics at the mobility edge in two- and three-dimensional systems,” *Phys. Rev. B*, vol. 59, pp. 9714–9717, Apr 1999.
- [128] B. Kramer, T. Ohtsuki, and S. Kettemann, “Random network models and quantum phase transitions in two dimensions,” *Physics reports*, vol. 417, no. 5-6, pp. 211–342, 2005.
- [129] K. Kobayashi, T. Ohtsuki, H. Obuse, and K. Slevin, “Conductance distributions in disordered quantum spin-hall systems,” *Physical Review B*, vol. 82, no. 16, p. 165301, 2010.

VITA

Dongwei Xu

Candidate for the Degree of

Doctor of Philosophy

Dissertation: DISORDER EFFECT IN GRAPHENE AND TOPOLOGICAL INSULATOR

Major Field: Physics

Biographical:

Personal Data: Born Yixian, Hebei, China on March 4th, 1982.

Education:

Received the B.S. degree from Lanzhou University, Lanzhou, Gansu, China, 2005, in Material Physics.

Received the M.S. degree from Lanzhou University, Lanzhou, Gansu, China, 2007, in Condensed Matter of Physics

Completed the requirements for the degree of Doctor of Philosophy with a major in Physics from Oklahoma State University in July, 2012.

Experience:

Working as Teaching Assistance from August 2007 to April 2010 and January 2011 to April 2011

Working as Research Assistance from May 2010 to December 2010 and May 2011 to July 2012

Professional Membership:

American Physical Society

Name: Dongwei Xu

Date of Degree: July, 2012

Institution: Oklahoma State University

Location: Stillwater, Oklahoma

Title of Study: DISORDER EFFECT IN GRAPHENE AND TOPOLOGICAL INSULATOR

Pages in Study: 86

Candidate for the Degree of Doctor of Philosophy

Major Field: Physics

Scope and Method of Study:

Disorder effect on graphene and topological insulators are the main focuses in this dissertation. Tight-binding model is mainly used to carry out the research. The disorder effect is modeled by introducing random distributed energies in a certain interval. The electron transport properties are studied using non-equilibrium Green's function method. Firstly, disorder induced field effect transistor (FET) in biased bilayer and trilayer graphene is proposed. A full band model Hamiltonian for multilayer graphene is employed to disclose the physical mechanism responsible for the disorder induced FET. Secondly, we study the disordered topological Anderson insulator (TAI) in a 2-D square geometry. Besides tight-binding model, effective medium theory (SCBA) is employed to predict the phase boundary.

Findings and Conclusions:

In the study of FET in biased multilayer graphene, the substrate is modeled by including disorder in the bottom graphene layer. The disorder effect on the conductance depends on the direction of the bias voltage. The ratio of conductances under opposite bias voltages is obtained, and it increases with disorder strength and voltage magnitude. The high peaks of the conductance ratio suggest that disorder can increase the FET efficiency. In this proposed FET, an energy gap is not required for the 'off' state. In the study of disordered TAI, we report the phase diagram of finite systems and study the evolution of phase boundaries with the increase of the system size. We establish that conductance quantization can occur without a bulk band gap, and that there are two distinct scaling regions with quantized conductance: TAI-I with a bulk band gap, and TAI-II with localized bulk states. We show that there is no intervening insulating phase between the bulk conduction phase and quantized regions, and that there is no metallic phase at the transition between the quantized and insulating phases. In a large portion of the conductance plateau eigenstates grow when the disorder strength is increased. The fractal dimension at the peak maximum is $d_2 \approx 1.5$. We report conductance distributions near several phase transitions and compare them with critical conductance distributions for well-known models.

ADVISER'S APPROVAL: Dr. Xincheng Xie